Doctoral Dissertation (Abridged)

博士論文 (要約)

Study on limiting factors of efficiency in InGaP multiple-quantum-well solar cells and their optimum design

(InGaP多重量子井戸太陽電池の変換効率制限要因の検討と最適設計)

令和元年11月29日提出

指導教員：中野　義昭　教授

Department of Electrical Engineering and Information Systems, School of Engineering,

The University of Tokyo

東京大学大学院工学系研究科

電気系工学専攻

学籍番号： 37-177076

Hsiang-Hung Huang

黄　祥鴻

This page is intentionally left blank.

Table of Contents

Abstract ii

Acknowledgment iii

Chapter 1 Introduction 1

1.1 Overview 1

1.1.1 Shockley-Queisser limit 3

1.1.2 Multi-junction solar cells to exceed Shockley-Queisser limit 5

1.1.3 Significance of GaInP solar cells 6

1.1.4 What makes a good solar cell? 7

1.1.5 Can multiple-quantum wells improve efficiencies? 8

1.2 Research outline 10

1.3 Reference 11

Chapter 2 Fundamentals 14

2.1 Optical absorption of materials 14

2.2 Carrier escape from quantum wells 16

2.3 Strain effects on strained hetroepitaxy layers 18

2.4 Essence knowledge on epitaxial layers 23

2.4.1 Thermodynamics of Epitaxial Growth 23

2.4.2 Critical thickness 27

2.4.3 Miscibility gap 30

2.4.4 Strain-balanced Criteria 31

2.5 Ordering effects on InGaP alloy 34

2.6 Reference 39

Chapter 3 Experiment equipment 41

3.1 Metal-Organic Vapor Phase Epitaxy (MOVPE) 41

3.2 X-ray diffraction (XRD) 42

3.3 Solar simulator 44

3.4 Reference 45

List of Publications 46

Abstract

It has been suggested that multiple-quantum-well (MQW) solar cells reveal a superior radiative emission nature than the bulk solar cell, implying a possibility of improving the conversion efficiency with a seemingly-enhanced output voltage. Meanwhile, carrier transport in MQW suffers due to the potential barriers of the hetero-structures in general, which implies a degraded output current. Several factors that limit the efficiency must be taken into account when one attempts to design MQW solar cells. On the other hand, in the previous research, MQW cells and bulk cells had been compared in an unfair manner due to their unidentical optical absorption thresholds. Furthermore, the complexity of designing MQWs targeting at a particular wavelength is rather high, because there are at least four parameters to investigate: the well material, the barrier material, the well thickness, and the barrier thickness.

In this dissertation, we are interested in exploring the optimum MQW design as well as the limiting factors of the efficiency of InGaP solar cells. In chapter 2, fundamental knowledge related to this research are firstly summarized, which is followed by a brief introduction of the experimental equipment and their basic principles in chapter 3.

In chapter 4, in order to explore an optimum MQW design for multijunction solar cells, a general design guideline for strain-balanced MQWs at a targeted absorption threshold based on carrier transport analysis is proposed. The critical mobility for maintaining an acceptable level of the degraded carrier transport as a QW solar cell is estimated. Its validity is further examined by comparing it with a QW solar cell design derived by an epitaxial growth strategy.

In chapter 5, by applying the InGaP/InGaP strain-balanced MQW designs derived in chapter 4, we make a fair comparison among the optimum solar cell designs that provide their maximum available conversion efficiency. The limiting factors of the efficiency of the MQW solar cell are discussed.

In chapter 6, the applications of the general design guideline for the strain-balanced MQW device is demonstrated. By growing a strain-balanced InGaP/InGaP design for multi-junction solar cells and a strain-balanced InGaAs/GaAsP design for a photonic power converter, we validate the fidelity of the proposed general design framework.

Acknowledgment

I am deeply indebted to my advisor, Prof. Y. Nakano, for giving me this amazing opportunity to work under his supervision at UTokyo. I value all what Prof. Y. Nakano has taught me through encouraging me, and through allowing me to do research independently. Whenever I needed any help, with his patience, Prof. Y. Nakano has always been there, providing all sorts of kind support. I could not have persisted until the very last moment if it weren't for your kindness and supervision. I would like to sincerely express my gratitude to my co-advisor, Prof. M. Sugiyama, who has guided me via commenting on various essential points regarding my research. With his immense knowledge, I have been inspired so profoundly that I could finally increase the completeness of this research. Thank you all for helping me grow into the researcher that I am today. Undoubtedly, my research could never have happened if it weren't for your guidance.

Besides my advisors, I would like to thank my advisory committee, Prof. Y. Okada, Assoc. Prof. T. Tanemura, and Assoc. Prof. N. Ahsan, for their insightful comments and encouragement. I am greatly respectful for their research, and I am thankful that they agreed to serve on my committee.

My sincere thanks also go to Prof. K. Hinzer and Dr. M. Wilkins for providing me an amazing opportunity to work on the multidisciplinary collaboration project.

I would like to thank all current and former members of the Nakano-Sugiyama-Tanemura group who helped me greatly to progress with my research, and supported my unforgettable journey in Japan. I would like to thank Dr. K. Toprasertpong and Dr. A. Delamarre, for being a tutor, a mentor, and a role model for me. I would like to thank Dr. B. Kim for teaching me how to use MOCVD for my research and being a reliable senpai. I would like to thank Dr. H. Sodabanlu, for kindly instructing me on doing device processes, and for serving as a reliable research consultant to me. I would like to thank Dr. K. Watanabe, and Dr. W. Yanwachirakul, for their technical assistance. I would like to thank Mr. H. Xu, and Ms. K. Feng, for helping me go through my difficult time. I would like to thank Dr. J. Zhang, Dr. Y. Xiao, Mr. R. Tang, Dr. J.-Q. Zhang, Dr. A.-B. Ren, Mr. Y.-Q. Wang, and Mr. P. Zhou, for being so supportive when I needed help. I would like to thank Ms. S. A. Emara, Dr. S. Lange, Dr. K. Ghosh, Mr. A. Reddy,

Mr. Y. Imazeki, Dr. M. A. Kazi, Mr. M. Giteau from Okada lab., and Mr. J. Z. Sun from UCSD, for sharing an enjoyable life in the lab with me. I would like to thank Dr. M. Nishimoto, Mr. M. Fukuda, Mr. T. Nakata, Mr. M. Kono, Mr. Y. Suganuma, Mr. T. Maruyama, Mr. S. Onozuka, Mr. M. Ogasawara, Mr. R. Tanomura, Mr. T. Fukutani, and Mr. M. Asami, for helping with my job hunting. I would like to thank Mr. T. Fukui, Miss R. Tsuchiya, and Miss M. Ito, for joining me on a nice trip to Beijing.

Special thanks to Mr. E. Kato, secretaries Ms. Y. Mazunaga and Ms. K. Tadokoro. My journey in Japan would never have been as easy and as smooth without your generous hospitality.

This research was financially supported by the New Energy and Industrial Technology Development Organization (NEDO), Japan: The Research and Development of Ultra-High Efficiency and Low-Cost III-V Compound Semiconductor Solar Cell Modules project (P15003). I would like to acknowledge full-scholarship support from Japan-Taiwan Exchange Association for 4-years.

Last but not least, I would like to thank my beloved family, my father, Chien-Ming Huang and my mother, Cheng-Ju Ho, for having my welfare as a top priority in their life, and for their unconditional love.

Hsiang-Hung Huang

Chapter 1 Introduction

1.1 Overview

The tremendous amount of excessive heat to the earth and several notorious green-house gases have been largely released by consuming fossil fuels such as oil, coal, and natural gas, owing to the rapid development of industry and increasing demand for electricity worldwide. However, these naturally-available resources are in limited supply, which causes the energy crisis, especially in nations that are poor in fossil resources. What's worse, massive usage of fossil fuels may have not only accelerated the process of global warming but also launched various irreversible environmental devastation to the earth as our home. As witnessed by signs in recent years, there is the increasingly frequent surge of large, destructive forest wildfires that destroy the ecosystem and burn down forests in Australia, California, and Amazon. A transformative massive ice melt has been observed in Greenland and Antarctica. Urgent protection protocols to mitigate such global devastations have become more demanded than ever and must be done.

Although there are challenges on low conversion efficiencies and power generation costs remaining, solar energy based on photovoltaic devices has been regarded as one of the safest, sustainable, environmentally-friendly renewable energy supplies. The efficiencies of various significant technologies in photovoltaics are summarized in Figure 1. 1. Crystalline silicon is the mainstream in the current market. In addition to the solar panel based on crystalline silicon (c-Si), there are other promising technologies such as single-junction GaAs cells, multi-junction cells, thin-film technologies, and the other emerging photovoltaics. Despite the immature technology, thin-film solar cells have the greatest advantages of low manufacturing processes and low material consumption. Relying on different photovoltaic substances with higher light absorption such as amorphous silicon (a-Si), cadmium telluride (CdTe), and copper indium gallium selenide (CIGS), it is suggested that the material cost can be 100 times much less than conventional solar cells made from crystalline materials. CIGS cell, for example, varies its bandgap value between 1.0–1.7 eV with the material content and has marked a record efficiency of 23.4 %. Nevertheless, outdoor usage of such cell causes severe light-induced degradation. Toxic ions diffuse out of the deposited semiconductor onto the

support glass under illumination particularly, which may lead to undesirable contamination to the environment though.

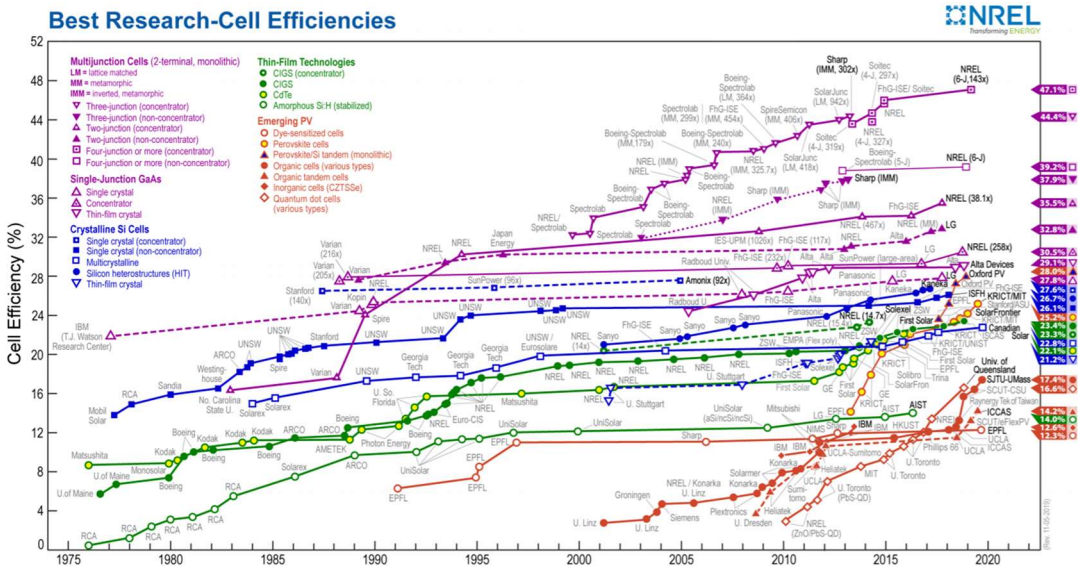

Figure 1. 1 A summary of the best research-cell efficiencies of various significant technologies provided by the National Renewable Energy Laboratory (NREL) [1]. The efficiencies are confirmed independently by institutions, e.g., NREL, AIST, JRC-ESTI, and Fraunhofer-ISE.

The recent breakthrough that occurred in the emerging photovoltaics is the research on perovskite materials. One of the most commonly-studied perovskite materials is the methylammonium lead trihalide ($CH_3NH_3PbX_3$. X represents a halogen element of use), with bandgap between 1.5–2.3 eV controlled by the halide content. Such novel materials demonstrate superior light absorption, carrier lifetimes, and mobilities, ensuring high conversion efficiencies with great opportunities to implement a low-cost, industry-scalable technology. Starting from 2013 with efficiency around 13 %, the efficiency has been rapidly boosted to a record 25% in 2019, which is comparable to the long-developed crystalline silicon technologies of 26.7% under one-sun illumination. One great challenge in perovskite solar cells is their chemical stability and reliability issue. Due to the water-solubility of the constituent organic absorber material, devices experience rapid degradation in moist environments, especially. Yet, featuring with low cost and high performance comparable to the commercially-available crystalline Si solar cells, perovskites have gathered a great deal of attention in both industry and a wide variety of research fields in recent years.

1.1.1 Shockley-Queisser limit

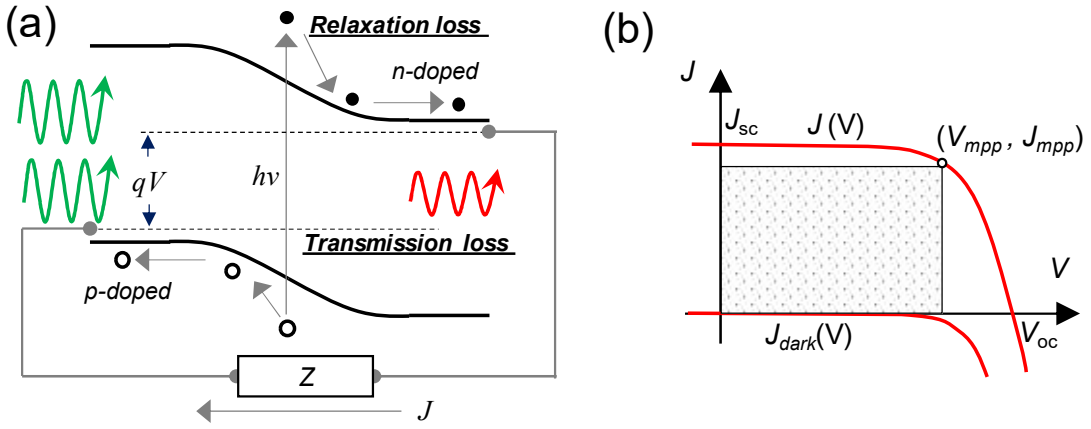

Figure 1. 2 (a) A schematic of the band diagram of an ideal Shockley-Queisser (SQ) diode as a solar cell (b) Typical current-voltage characteristics of a solar cell [2], [3]. qV is the quasi-Fermi level splitting.

Single-junction solar cell based on III-V compound semiconductor GaAs has revealed a remarkable energy yield of 27.8 % close to the so-called radiative limit of 32.6 % anticipated by Shockley and Queisser on the basis of detailed balance analysis in 1961 [4]. According to the theory, some relevant fundamental assumptions to estimation the efficiency of a p-n junction as a solar cell, are:

(1) Carriers have infinite mobility, which enables a complete carrier separation and collection wherever they are generated.

(2) Zero reflectivity. The absorptance above the bandgap is 100 %, whereas below is 0 %.

(3) The electron-hole pairs relax to the band edges immediately as they are generated. The temperature of the p-n junction reaches thermal equilibrium with its ambient environment.

(4) Radiative recombination, modeled by the black-body radiation, is the only recombination loss mechanism. The associated quasi-Fermi level-splitting is uniformly distributed across the solar cell.

As a result, the current-voltage curve under illumination in the SQ limit follows as:

$$J = J_{sc}^{SQ} - J_0^{SQ}\left(e^{\frac{qV}{k_B T}} - 1\right), \tag{1. 1}$$

where J_{sc}^{SQ} is the short-circuit current and J_0^{SQ} is the so-called saturation current density due to radiative loss. The second term is also known as the dark current Figure 1. 2 shows the band

structure and the *J-V* characteristics of an ideal SQ-diode.

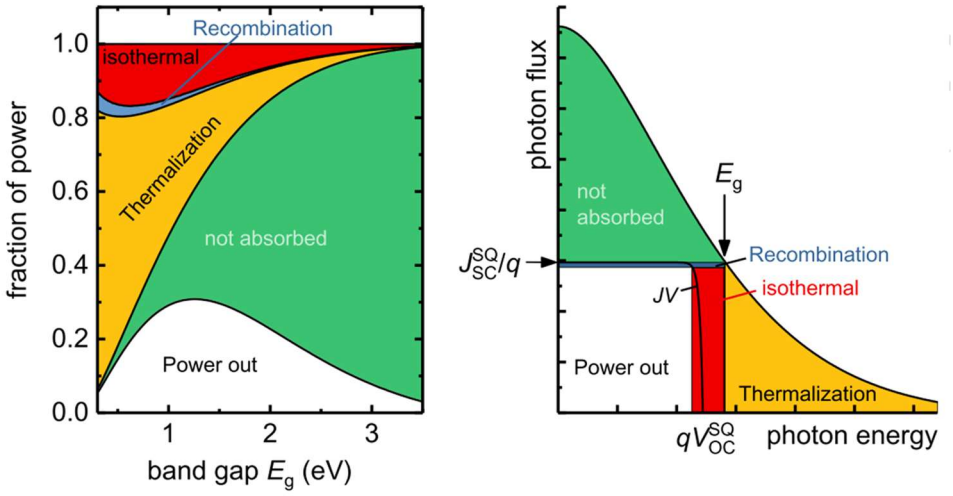

Figure 1. 3 The fraction of power of an ideal Shockley-Queisser (SQ), adapted from [5], [6].

The conversion efficiency of an ideal SQ-diode is hence estimated by dividing the output power at the maximum power point (*MPP*) with the incident spectral power. The dependence of the fraction of power generation on the bandgap of the absorber is shown in Figure 1. 3. Fundamentally, an ideal SQ-diode suffers from the transmission loss (green area), the relaxation loss (or, thermalization loss, the yellow area), and the ‘‘isothermal dissipation’’ loss due to carrier collection of the electron-hole pair[6]. The isothermal dissipation loss refers to the loss of potential energy as it generates heat in the solar cell without a change of the temperature of electrons and holes, and the carriers do not recombine. Designs that exceed the Shockley–Queisser limit work by overcoming one or more of these three loss processes.

It should be noticed that a more general form taking into account arbitrary absorption profile, limited mobilities, non-radiative recombination can be expressed as follows[2], [3], [7]:

$$J = J_{SC} - J_0^{rad}\left(e^{\frac{qV}{k_BT}} - 1\right) - J_{01}\left(e^{\frac{qV}{k_BT}} - 1\right) - J_{02}\left(e^{\frac{qV}{2k_BT}} - 1\right), \quad (1.2)$$

where J_{SC} and J_0^{rad} are the diminished short-circuit current and radiative current due to the imperfection of materials. J_{01} and J_{02} are the non-radiative saturation currents with the ideality factor of 1 and 2, respectively.

1.1.2 Multi-junction solar cells to exceed Shockley-Queisser limit

Among the third generation of new types of solar cells, the multi-junction solar cells (MJSCs), also known as the tandem solar cells, not only have been successfully achieved efficiency over 40% but also keep breaking the efficiency record year-by-year. By staking single-junction solar cells with distinctive bandgaps in a decreasing order to absorb more photons from the solar spectrum, both the transmission and relaxation loss can be substantially reduced. In this case, dividing the spectrum equally, the output current reduces while the output voltage is greatly promoted as the stacked absorbers increase, resulting in efficiencies that exceed the Shockley-Queisser limit for single-junctions. Due to the extraordinary electronic properties, direct bandgap nature, and easier integration by using epitaxial growth, tandem sells composed of III-V semiconductors have been the mainstream over the past years. Typical architectures of such photovoltaics and their conversion efficiencies are presented in Figure 1. 4.

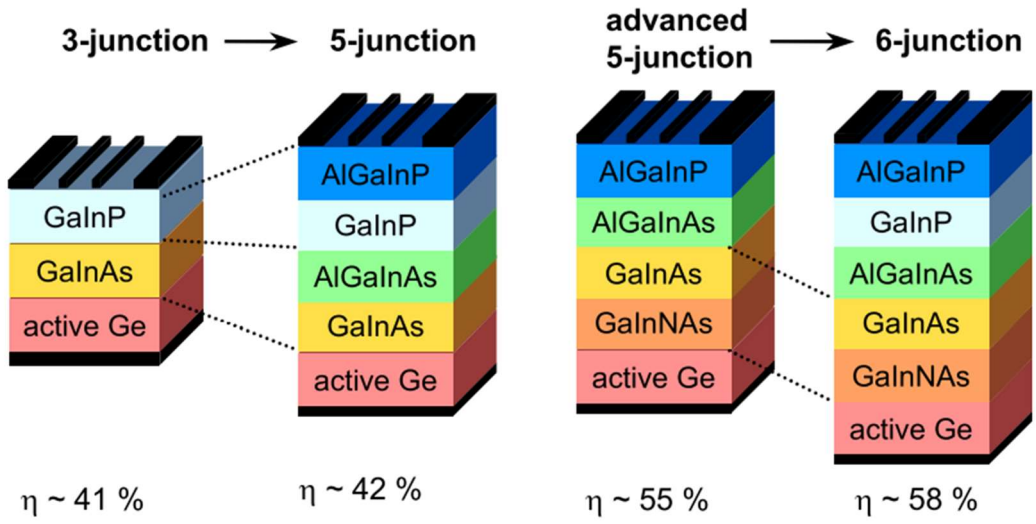

Figure 1. 4 Multi-junction solar cells (MJSCs) based on III-V compound semiconductors on an active Ge substrate and their corresponding theoretical efficiencies [8].

In 2019, a six-junction solar cell made by employing an inverted-metamorphic (IMM) architecture with AlGaInP/AlGaAs/GaAs/GaInAs(3) (2.15/1.72/1.41/1.17/0.96/0.70 eV) has achieved a record efficiency 47.1% under 143-suns remarkably [9]. Although challenges such as cost reduction remain, their high efficiencies and long-term stability ensure applications in space systems.

1.1.3 Significance of GaInP solar cells

As shown in Figure 1. 4, because of its large bandgap and lattice-matched nature, GaInP (1.82-1.91 eV) has been widely applied to top cells for the MJSC technology. Figure 1. 5 demonstrates the external quantum efficiency (EQE) and the current-voltage characteristics of the record GaInP single-junction cell, where the open-circuit voltage is 1.49 V, short-circuit current is 16.31, and the conversion efficiency is 21.4% [10]. The SQ-limit of the GaInP solar cell with bandgap 1.91 eV is around 25%. This suggests that there are rooms for pushing the conversion efficiency toward the limit, which is critical for further enhancing the efficiency of an MJSC based on a GaInP device as a whole.

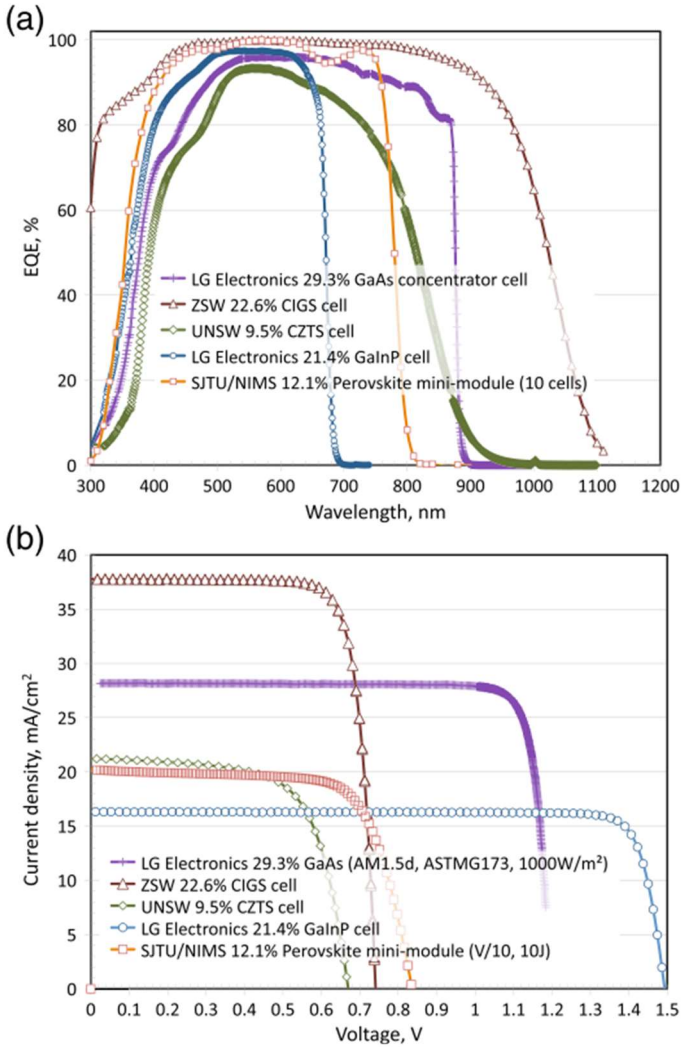

Figure 1. 5 The external quantum efficiency (EQE) and the current-voltage characteristics of the record GaInP single-junction cell and other significant photovoltaic devices [10].

1.1.4 What makes a good solar cell?

The approach for improving the efficiency of a solar cell, in general, can be studied from its internal parameters, such as the absorption coefficient, the mobility, the lifetime, and internal quantum efficiency as a light-emitting diode (LED)[7]. For example, it has been pointed out that luminescence efficiency, or radiative efficiency, of a solar cell, can possess a critical impact on its conversion efficiency by O. D. Miller *et al.*[11] and U. Rau [12]. Figure 1. 6(a) displays the dependence of conversion efficiency on non-100% internal radiative efficiencies. It can be observed that a drop of radiative efficiency from 100% to 90% leads to severely degraded performance, whereas a drop from 90% to 80% leads to little additional impact. With sufficient internal radiative efficiency, photons due to radiative recombination inside gain a better chance to overcome total internal reflection and escape from the solar cell, which contributes to a better quasi-Fermi level splitting and thereby a larger output voltage. On the contrary, with limited internal radiative efficiency, the emitted photons are trapped by total internal reflection readily. In this case, they experience a higher chance of dissipated as heats due to some parasitic loss effects, resulting in a poor output voltage.

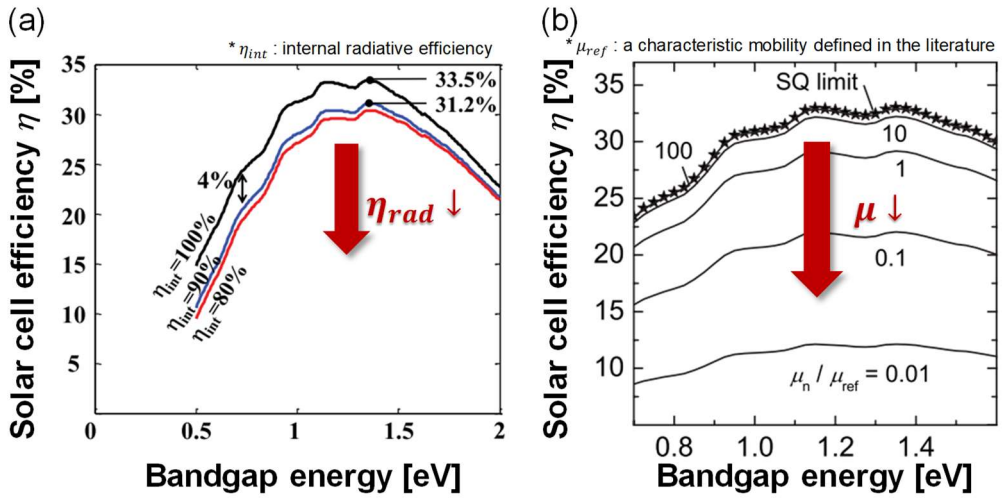

Figure 1. 6 (a) The conversion efficiency versus bandgap under non-100% radiative efficiencies (red and blue curves, the $\eta_{int.}$ denotes for internal radiative efficiency) [11]. (b) The conversion efficiency versus bandgap under finite mobilities for carrier transport [13], where mn represents the electron mobility, and μ_{ref} represents the characteristic mobility used for solving the Poisson-Drift-Diffusion equations in the literature.

With only 2% escaping per emission event, even a 90% internal luminescence yield on each cycle would appear inadequate [11]. Since a good solar cell should also be a good LED [12], promoting radiative efficiency toward 100% provides a hint to improve the output voltage of solar cells.

On the other hand, carrier transport in terms of mobility plays a crucial role in carrier collection for generating the output current, as shown in Figure 1. 6(b). The Shockley-Queisser limit is denoted by the stars in the figure. It can be preserved that a drop in carrier mobility is accompanied by a drop in conversion efficiency. Even if the recombination mechanism of carriers is assumed to be purely radiative, the conversion efficiency diminishes drastically, suffering from a reduced carrier collection as well as a limited short circuit current. Satisfactory carrier transport is demanded in carrier collection for the output current.

1.1.5 Can multiple-quantum wells improve efficiencies?

Thanks to an engineerable optical absorption threshold, solar cells based on multiple-quantum-wells (MQWs) have been proposed as a flexible technique to ensure current matching for multi-junction solar cells [14]. For example, a 1.15-eV MQW design based on InGaAs/GaAsP for quad-junction solar cells toward 50.1% conversion efficiency has been developed successfully [15]. Such design not only reveals an optimum optical absorption threshold for the MJSC but also is compatible with a successive epitaxial growth with other subcells on a Ge substrate, suggesting a promising candidate to improve the efficiency for MJSCs as a whole device.

In addition to bandgap engineering, quantum-well structures have been applied to various optical active devices such as laser diodes and LEDs because of their high radiative efficiency nature. Since a solar cell with high radiative efficiency suggests a close operation with an ideal Shockley-Queisser diode, quantum-well solar cells (QWSCs) may provide a new route to realizing an ideal Shockley-Queisser diode. Figure 1. 7 shows a comparison between a *p-i-n* QWSC based on a 50-periods InGaAs/GaAsP quantum-well design and a reference *p-i-n* GaAs solar cell [16].

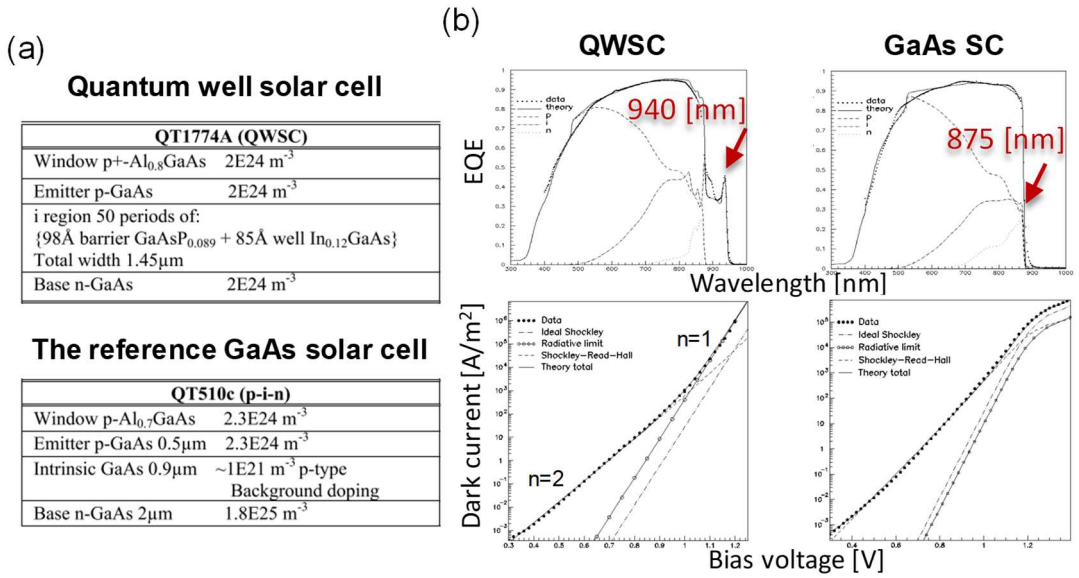

Figure 1. 7 (a) A *p-i-n* quantum-well solar cell (QWSC) and a *p-i-n* GaAs reference solar cell. (b) The external quantum efficiency (EQE) and the dark current of the solar cell designs. Figures are adapted from Ref. [16].

From the external quantum efficiency (EQE) measurement results, the optical absorption threshold of the QWSC is located at 940 nm, whereas that of the reference GaAs cell is located at 875 nm. Although the transition edges start at distinctive wavelengths, it is observed that the ideality factor of the dark current switches from 2 to 1 from ~10^3 mA/cm^2 for the QWSC, while even at ~10^4 mA/cm^2, where the series resistance comes into play, the ideality factor holds 2 for the reference GaAs cell. This indicates that the QWSC, in this case, behave a closer characteristic to an ideal Shockley-Queisser diode than the GaAs reference cell.

Another relevant previous research in which MQW solar cells with different periods are compared with a GaAs reference cell is displayed in Figure 1. 8. In this research, the MQW solar cells demonstrate 1-order-of-magnitude higher external radiative efficiency than the GaAs reference cell, which reveals their highly-radiative nature than the bulk reference. Although the measurement results of the open-circuit voltage remain lower than that of the bulk reference, the highly-radiative nature suggests a possibility to achieve a better output voltage toward the Shockley-Queisser limit.

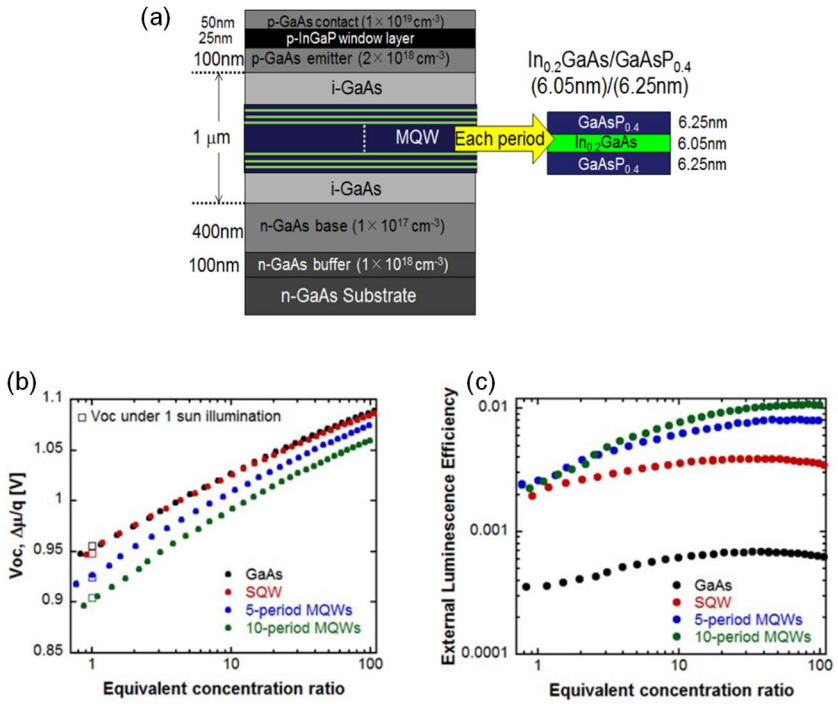

Figure 1. 8 (a) A *p-i-n* strain-balanced quantum-well solar cell design. (b) The open-circuit voltage V_{oc} as a function of equivalent concentration ratio (c) The external radiative (luminescence) efficiency as a function of equivalent concentration ratio. This figure is adapted from Ref. [17].

1.2 Research outline

It has been suggested that multiple-quantum-well (MQW) solar cells reveal a superior radiative emission nature than the bulk solar cell, implying a possibility of improving the conversion efficiency with a seemingly-enhanced output voltage. Meanwhile, carrier transport in MQW suffers due to the potential barriers of the hetero-structures in general, which implies a degraded output current. Several factors that limit the efficiency must be taken into account when one attempts to design MQW solar cells. On the other hand, in the previous research, MQW cells and bulk cells had been compared in an unfair manner due to their unidentical optical absorption thresholds. Furthermore, the complexity of designing MQWs targeting at a particular wavelength is rather high, because there are at least four parameters to investigate: the well material, the barrier material, the well thickness, and the barrier thickness.

In this dissertation, we are interested in exploring the optimum MQW design as well as the limiting factors of the efficiency of InGaP solar cells. In chapter 2, fundamental knowledge related to this research are firstly summarized, which is followed by a brief introduction of the experimental equipment and their basic principles in chapter 3.

In chapter 4, in order to explore an optimum MQW design for multijunction solar cells, a general design guideline for strain-balanced MQWs at a targeted absorption threshold based on carrier transport analysis is proposed. The critical mobility for maintaining an acceptable level of the degraded carrier transport as a QW solar cell is estimated. Its validity is further examined by comparing it with a QW solar cell design derived by an epitaxial growth strategy.

In chapter 5, by applying the InGaP/InGaP strain-balanced MQW designs derived in chapter 4, we make a fair comparison among the optimum solar cell designs that provide their maximum available conversion efficiency. The limiting factors of the efficiency of the MQW solar cell are discussed.

In chapter 6, the applications of the general design guideline for the strain-balanced MQW device is demonstrated. By growing a strain-balanced InGaP/InGaP design for multi-junction solar cells and a strain-balanced InGaAs/GaAsP design for a photonic power converter, we validate the fidelity of the proposed general design framework.

1.3 Reference

[1] NREL, "Photovoltaic Research | NREL," *Nrel*, 2017. [Online]. Available: https://www.nrel.gov/pv/.

[2] J. Nelson, *The Physics of Solar Cells*, vol. 50, no. 8. PUBLISHED BY IMPERIAL COLLEGE PRESS AND DISTRIBUTED BY WORLD SCIENTIFIC PUBLISHING CO., 2003.

[3] "PVEducation." [Online]. Available: https://www.pveducation.org/.

[4] W. Shockley and H. J. Queisser, "Detailed balance limit of efficiency of p-n junction solar cells," *J. Appl. Phys.*, vol. 32, no. 3, pp. 510–519, 1961.

[5] "Shockley–Queisser limit - Wikipedia." [Online]. Available: https://en.wikipedia.org/wiki/Shockley–Queisser_limit.

[6] J. F. Guillemoles, T. Kirchartz, D. Cahen, and U. Rau, "Guide for the perplexed to the Shockley–Queisser model for solar cells," *Nature Photonics*, vol. 13, no. 8. pp. 501–505, 28-Mar-2019.

[7] T. Kirchartz and U. Rau, "What Makes a Good Solar Cell?," *Adv. Energy Mater.*, vol. 1703385, 2018.

[8] A. W. Bett, C. Baur, F. Dimroth, W. Guter, M. Meusel, and G. Strobl, "Recent developments in III-V multi-junction space solar cells," *Eur. Sp. Agency, (Special Publ. ESA SP*, no. 589, pp. 25–30, 2005.

[9] M. A. Green, E. D. Dunlop, J. Hohl-Ebinger, M. Yoshita, N. Kopidakis, and A. W. Y. Ho-Baillie, "Solar cell efficiency tables (Version 55)," *Prog. Photovoltaics Res. Appl.*, vol. 28, no. 1, pp. 3–15, Jan. 2020.

[10] M. A. Green *et al.*, "Solar cell efficiency tables (version 49)," *Prog. Photovoltaics Res. Appl.*, vol. 25, no. 1, pp. 3–13, Jan. 2017.

[11] O. D. Miller, E. Yablonovitch, and S. R. Kurtz, "Strong Internal and External Luminescence as Solar Cells Approach the Shockley–Queisser Limit," *IEEE J. Photovoltaics*, vol. 2, no. 3, pp. 303–311, Jul. 2012.

[12] U. Rau, "Reciprocity relation between photovoltaic quantum efficiency and electroluminescent emission of solar cells," *Phys. Rev. B - Condens. Matter Mater. Phys.*, vol. 76, no. 8, pp. 1–8, 2007.

[13] J. Mattheis, J. H. Werner, and U. Rau, "Finite mobility effects on the radiative efficiency limit of pn-junction solar cells," *Phys. Rev. B*, vol. 77, no. 8, p. 085203, 2008.

[14] K. W. J. Barnham and G. Duggan, "A new approach to high-efficiency multi-band-gap solar cells," *J. Appl. Phys.*, vol. 67, no. 7, pp. 3490–3493, 1990.

[15] K. Toprasertpong *et al.*, "Absorption threshold extended to 1.15 eV using InGaAs/GaAsP quantum wells for over-50%-efficient lattice-matched quad-junction solar cells," *Prog. Photovoltaics Res. Appl.*, vol. 24, no. 4, pp. 533–542, Apr. 2016.

[16] J. Connolly, I. Ballard, K. Barnham, D. B. Bushnell, T. N. D. Tibbits, and J. S. Roberts, "Efficiency limits of quantum well solar cells," *19th Eur. Photovoltaics Energy Conf.*, vol. 75005, no. June, pp. 355–358, 2004.

[17] T. Inoue *et al.*, "Quasi-Fermi level splitting evaluation based on electroluminescence analysis in multiple quantum-well solar cells for

investigating cell performance under concentrated light," in *Proceedings of Spie - the International Society for Optical Engineering*, 2016, vol. 9743, no. March, p. 974316.

Chapter 2 Fundamentals

In this chapter, fundamental knowledges regarding optical absorption, carrier transport, strain effects on the electronic properties of epitaxial layers, thermodynamics of crystal growth, critical layer thickness for avoiding defect generations in epilayers, strain-balance conditions reducing the average strain for realizing a thermodynamically-stable multiple-quantum-wells (MQWs), and the atomic ordering effects on InGaP alloys.

2.1 Optical absorption of materials

Optical responses, such as the refractive index, extinction coefficient, and absorption coefficient are essential for determining the device performance of photovoltaics. For examples, the photon-generation rate of carriers follows the Beer–Lambert law, which requires the information of the optical absorption coefficient. Reflectivity of the solar cell is evaluated by the refractive indices. Here, essential formulae for evaluating the absorption coefficient of bulk material in this research are summarized [1], [2].

Given the complex dielectric function:

$$\varepsilon(\omega) = \varepsilon_1(\omega) + i\varepsilon_2(\omega)\ , \tag{2. 1}$$

, the complex refractive index is derived by:

$$n^*(\omega) = \ \varepsilon(\omega)^{1/2} = n(\omega) + ik(\omega)\ , \tag{2. 2}$$

where $n(\omega)$ is the real part of the refractive index, and $k(\omega)$ is the attenuation coefficient, or, the so-called attenuation coefficient. It should be noticed that these two quantities can be determined by optical measurements. Based on the above expressions, $n(\omega)$ and $k(\omega)$ are written by:

$$n(\omega) = \left(\frac{\left[\varepsilon_1(\omega)^2 + \varepsilon_2(\omega)^2\right]^{1/2} + \varepsilon_1(\omega)}{2} \right)^{1/2}, \tag{2. 3}$$

$$k(\omega) = \left(\frac{\left[\varepsilon_1(\omega)^2 + \varepsilon_2(\omega)^2\right]^{1/2} - \varepsilon_1(\omega)}{2} \right)^{1/2}, \tag{2. 4}$$

The absorption coefficient is evaluated by the attenuation coefficient:

$$\alpha(\omega) = \frac{4\pi k(\omega)}{\lambda} = \frac{4\pi}{\lambda}\left(\frac{\left[\varepsilon_1(\omega)^2 + \varepsilon_2(\omega)^2\right]^{1/2} - \varepsilon_1(\omega)}{2}\right)^{1/2}, \qquad (2.5)$$

where λ is the wavelength in the vacuum. Additionally, both the real part and the imaginary part of the complex dielectric function are related by the Kramers–Kronig relations as follows [3]:

$$\varepsilon_1(\omega) = 1 + \frac{2}{\pi}\int_0^{\infty} \frac{\omega'\varepsilon_2(\omega')}{(\omega')^2 - \omega^2} d\omega' , \qquad (2.6)$$

$$\varepsilon_2(\omega) = -\frac{2}{\pi}\int_0^{\infty} \frac{\varepsilon_1(\omega')}{(\omega')^2 - \omega^2} d\omega' , \qquad (2.7)$$

The theoretical approach for estimating the complex dielectric function relies on evaluating $\varepsilon_1(\omega)$ given a known explicit form of $\varepsilon_2(\omega)$ by the above relation. The imaginary part of $\varepsilon(\omega)$ is strongly dependent on both the joint density-of-states function and the momentum matrix element. That is to say:

$$\varepsilon_2(\omega) = \frac{4\hbar^2 e^2}{\pi m^2 \omega^2} M_0^2 J_{cv}(\omega), \qquad (2.8)$$

where $\hbar$ is the reduced Planck constant, e is the unit charge, m is the unit electron mass, M_0 is the momentum matrix element for transitions from the conduction band to the valence band, and $J_{cv}(\omega)$ is the joint density-of-states. It is noted that $J_{cv}(\omega)$ is a significant quantity that can be used to interpret the behaviors of optical transitions in at various sorts of critical points (CPs) in the Brillouin zone [4].

For typical III-V compound semiconductors, such as GaAs, InP, GaP, InSb, AlGaAs, InGaAsP, …etc.), similar transition peaks can be identified in their optical spectra. Because these crystals are in a zinc-blende arrangement, the joint density-of-states $J_{cv}(\omega)$ for optical transitions derived by considering each significant critical point demonstrates a similar behavior. In this research, 4-kinds of significant transitions are taken into account for deriving the relevant optical properties.

(1) E_0 and $E_0 + \Delta_0$ transitions: The transition in the diamond- and zinc-blende-type semiconductors take place in the center of the Brillouin zone.
(2) E_1 and $E_1 + \Delta_1$ transitions: A sort of typical transitions in the InGaAsP quaternary alloys occurs at L-points or along the Λ-direction in the Brillouin zone.

(3) E_2 (E_0') transitions: This type of transitions appears more profound especially in the higher energy region above than the previous two types of transitions. Such transitions are believed to reveal at the Γ-point, or in the Λ-direction near the Γ-point.

(4) Indirect-band-gap transitions: Significant transitions at $E_g^X(\Gamma_8^v \rightarrow X_6^c)$ and $E_g^L(\Gamma_8^v \rightarrow L_6^c)$ are included in the model.

Figure 2. 1 shows an example of the theoretical $\varepsilon_2(\omega)$ compared with the measurement result of an $In_{0.52}Ga_{0.48}As$ layer. The aforementioned characteristic profiles are indicated by the arrows in the figure.

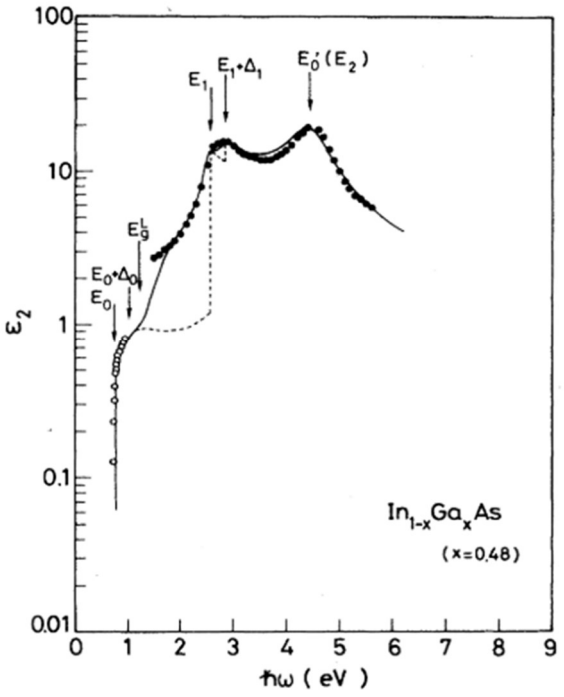

Figure 2. 1 The imaginary part of the complex dielectric function of an $In_{0.52}Ga_{0.48}As$ film [2].

2.2 Carrier escape from quantum wells

The escape probability functions for estimating the escape mechanisms of thermionic escape and tunneling escape are summarized below. These functions have been widely-employed for qualitatively analyzing the transport mechanism by which photo-carriers in the multiple-quantum-well structures are extracted in some previous research [5]–[8].

Thermionic escape

For the carriers staying the quantum wells with quantized energies E_n, the thermionic-emission lifetime can be expressed as:

$$\frac{1}{\tau_{th.}} = \frac{1}{t_w}\sqrt{\frac{kT}{2\pi m_w^*}}\exp\left(-\frac{\Delta E_{C,V} - E_n - qFt_w/2}{k_B T}\right), \quad (2.9)$$

where t_w is the well thickness, m_w^* is the effective mass in the well layer, $\Delta E_{C,V}$ is the potential offset for carriers, E_n is the n-th confinement energy accessed from the center of the well, and F is the electric field. It is noticed that, the term $\Delta E_{C,V} - E_n - qFt_w/2$ represents the effective barrier height seen from the n-th confined state. Secondly, the derivation of this formula involves in assuming that carrier density is equal to the 3D carrier density of the well layer in the entire energy range. A more precise approximation should take into account the contribution from the confined carriers, especially as the barrier height is rather high so that the 3D carrier density becomes negligible. This expression suggests a higher escape probability from the well, which facilitates carrier extraction for photovoltaics.

Tunneling escape

Confined carriers in the n-th state of the wells can transport via direct tunneling escape. The tunneling lifetime of the carriers through a set of a well and a barrier tunnel is given by the product of the transmittance per barrier T and the inverse of the transport time per well. By using WKB approximation for the transmittance T, the tunneling lifetime is written in:

$$\frac{1}{\tau_{n,tun.\pm}} = \frac{1}{2t_w}\sqrt{\frac{2E_n}{m_{\perp n}^*}}\exp\left(-\frac{2}{\hbar}\int_0^{t_b}\sqrt{2m_b^*(\Delta E_{C,V} - E_n \mp (\frac{1}{2}t_w + z)qF)}\right) \quad (2.10)$$

where t_b is the barrier thickness, $m_{\perp n}^*$ is the perpendicular effective mass in the n-th state of the quantum well, and m_b^* is the barrier effective mass.

These two expressions provide basic intuition to distinguish the transport mechanism by which carriers are collected.

2.3 Strain effects on strained hetroepitaxy layers

When designing optoelectronic devices consisting of strained quantum wells or superlattices in particular, one must carefully take into account the effects caused by strain. For epitaxial layers pseudomorphically grown on a lattice-mismatched substrate, with external strain imposing on the epilayers, the atomic lattice is correspondingly deformed according to the elastic theory. As a result, the interaction of potential energies among atoms can either be dwindled or enhanced considerably, which is responsible for the modification of several electronic properties such as bandgap energies and effective masses compared to that of bulk materials. Figure 2. 2 illustrates an example showing the effects of strain on the conduction (C), heavy-hole (HH), light-hole (LH) band structure in the momentum space for a $Ga_xIn_{1-x}As$ epilayer grown on InP substrate under biaxial compression, lattice-matched condition, and biaxial tension.

In this section, we introduce the fundamental physics behind and the essential formulae based on perturbation theory and model-solid theory employed in this research.

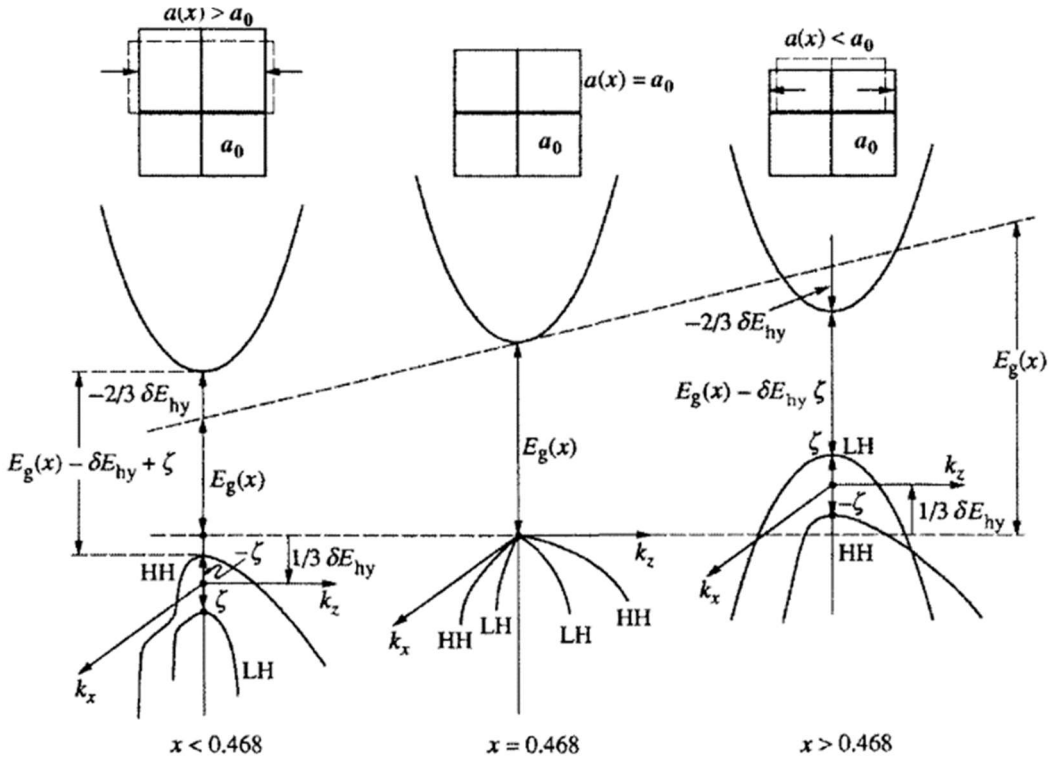

Figure 2. 2 Schematic diagram of how the band structure in the momentum space for a bulk $Ga_xIn_{1-x}As$ material under (a) biaxial compression, (b) no-strain (lattice-matched condition), and (c) biaxial tension for different composition ratio of gallium [9].

Bikus-Bir Hamiltonian

Assume that only biaxial strain present in the epilayer for simplicity, that is to say:

$$\epsilon_{xx} = \epsilon_{yy} \neq \epsilon_{zz}, \qquad \epsilon_{xy} = \epsilon_{yz} = \epsilon_{zx} = 0, \tag{2. 11}$$

where ϵ represents the subjected strain. This consideration fundamentally covers one of the most significant strained systems of our interest: a strained-layer semiconductor pseudomorphically grown a (001)-oriented substrate. To evaluate the strain for such a case in this sense, it follows the relations:

$$\epsilon_{xx} = \epsilon_{yy} = \frac{a_{sub} - a_{epi}}{a_{epi}}, \qquad e_{zz} = -\frac{2C_{12}}{C_{11}}\epsilon_{xx}, \tag{2. 12}$$

where a_{sub} and a_{epi} are the lattice constants of the substrate and the epitaxial layer, and C is for the elastic constant. ϵ_{zz} is derived by the stress tensor σ related to strain ϵ by the elastic stiffness tensor with the corresponding elastic constants C_{ij}.

Now, we solely focus on the six valence bands (i.e., all the doubly degenerate heavy-hole (HH), light-hole (LH), and spin-orbit split-off bands (SO)) and neglect the coupling to the two degenerate conduction bands with both spins. By considering the strain contributions, Bikus and Bir proposed a Hamiltonian for a strained semiconductor extended from the full 6×6 Luttinger-Kohn Hamiltonian for an unstrained semiconductor. If we further restrict ourselves to the circumstance that the band edge at $\mathbf{k} = 0$ in the momentum space, the Bikus-Bir Hamiltonian $\boldsymbol{H}$ then can be simplified to be:

$$\boldsymbol{H}(\mathbf{k}=0) = -\begin{bmatrix} P_\epsilon + Q_\epsilon & 0 & 0 & 0 & 0 & 0 \\ 0 & P_\epsilon - Q_\epsilon & 0 & 0 & -\sqrt{2}Q_\epsilon & 0 \\ 0 & 0 & P_\epsilon - Q_\epsilon & 0 & 0 & \sqrt{2}Q_\epsilon \\ 0 & 0 & 0 & P_\epsilon + Q_\epsilon & 0 & 0 \\ 0 & -\sqrt{2}Q_\epsilon & 0 & 0 & P_\epsilon + \Delta & 0 \\ 0 & 0 & \sqrt{2}Q_\epsilon & 0 & 0 & P_\epsilon + \Delta \end{bmatrix}, \tag{2. 13}$$

where P_ϵ is denoted for contribution from the hydrostatic strain deformation potential energy, Q_ϵ is for the contribution from shear strain deformation potential energy, and Δ is for the spin-orbit splitting energy. P_ϵ and Q_ϵ are obtained from the following expressions,

$$P_\epsilon = -a_v(\epsilon_{xx} + \epsilon_{yy} + \epsilon_{zz}), \qquad Q_\epsilon = -\frac{b}{2}(\epsilon_{xx} + \epsilon_{yy} - 2\epsilon_{zz}), \qquad (2.\ 14)$$

where a_v represents hydrostatic deformation potential for valance band, b represents the shear deformation potential. According to the model-solid theory, the volume change of the strained layer determines the hydrostatic contribution (P_ϵ) of the strain, and will enter into the overall band lineups. In contrast, the non-hydrostatic components (Q_ϵ) due to shear strains, which determine the uniaxial (or biaxial) strains, will cause splitting of degenerate bands.

By solving the eigenvalues for the above Hamiltonian $\boldsymbol{H}(\mathbf{k} = 0)$, the band-edge energies can be derived,

$$E_{HH}(\mathbf{k} = 0) = -P_\epsilon - Q_\epsilon, \qquad (2.\ 15)$$

$$E_{LH}(\mathbf{k} = 0) = -P_\epsilon + \frac{1}{2}\left(Q_\epsilon - \Delta + \sqrt{\Delta^2 + 2\Delta Q_\epsilon + 9Q_\epsilon^2}\right), \qquad (2.\ 16)$$

$$E_{SO}(\mathbf{k} = 0) = -P_\epsilon + \frac{1}{2}\left(Q_\epsilon - \Delta - \sqrt{\Delta^2 + 2\Delta Q_\epsilon + 9Q_\epsilon^2}\right), \qquad (2.\ 17)$$

Interestingly, it can be readily observed that the spin-orbit splitting contribution Δ is decoupled from the heavy-hole band, whereas the light-hole band edge is coupled with the spin-orbit splitting.

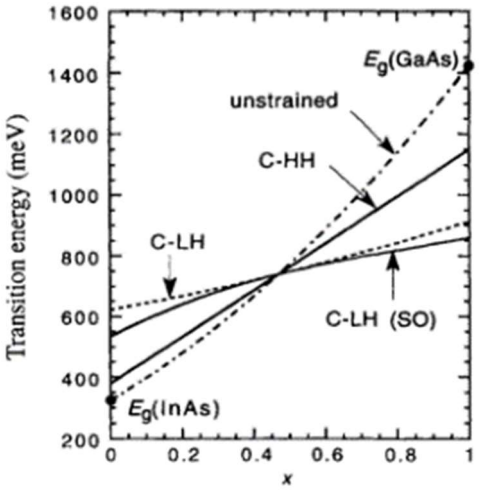

Figure 2. 3 The bandgap energy of an $In_{1-x}Ga_xAs$ layer with the composition ratio x ranging from 0 to 1 psudomorphically grown on an InP substrate. The solid curves represent the associated transition energies from the heavy-hole (HH) and light-hole (LH) band to the conduction band (C). The dashed curve is the transition energy from the light-hole band (LH) to the conduction (C) without the effect due to spin-orbit coupling (SO). The dotted-dashed curve is the transition energy of an unstrained $In_{1-x}Ga_xAs$ layer as a reference [9].

Figure 2. 3 shows the transition energies from HH, LH, and SO band to the conduction band evaluated by the above equations with the same example shown in Figure 2. 2. When x = 0.468, the layer material is lattice-matched to the InP substrate. It can be clearly seen that the transition energies, especially from HH and LH, deviate a few meV to ~100 meV from the unstrained bandgap energy, suggesting a non-negligible impact on the electronic properties in the presence of strain.

Please be aware that on the basis of Luttinger-Kohn model, the effective masses parallel (|| or t) or perpendicular (⊥ or z) to the interface of the substrate are attained by the Luttinger parameters γ from:

$$\frac{m_{hh}^{z}}{m_0} = \frac{1}{\gamma_1 - 2\gamma_2} \qquad \frac{m_{hh}^{t}}{m_0} = \frac{1}{\gamma_1 + \gamma_2}, \tag{2. 18}$$

$$\frac{m_{lh}^{z}}{m_0} = \frac{1}{\gamma_1 + 2\gamma_2} \qquad \frac{m_{lh}^{t}}{m_0} = \frac{1}{\gamma_1 - \gamma_2}, \tag{2. 19}$$

The longitudinal effective mass can be used to calculate the energy levels of quantum well. The transverse effective mass can be used to calculate 2D density of states, …etc.

Models for band alignment

Here, we summarize the detailed formulae taken from Krijn, quantifying the band-alignment of strained layers in this research. Although the expressions appear different from what introduced previously, they do not contradict the physics behind. In the following discussion, we mainly focus on strain effects that occur at the Γ-point of a Zincblende structure. Grown pseudomorphically on a (001)-oriented substrate with lattice constant a_{sub}, the epilayer with relaxed lattice constant a_{epi} is subjected to a biaxial strain $\epsilon_{\parallel}$ parallel to the plane of the interface and a uniaxial strain $\epsilon_{\perp}$ perpendicular to it:

$$\epsilon_{\parallel,\perp} = \frac{a_{\parallel,\perp}}{a_{epi}} - 1, \tag{2. 20}$$

where the deformed lattice constants follow the relations:

$$a_{\parallel} = a_{sub}, \qquad a_{\perp} = a_{epi}\left(1 - 2\frac{C_{12}}{C_{11}}\epsilon_{\parallel}\right). \tag{2. 21}$$

Here, C represents the elastic constant. Note that the subscript || is equivalent to xx and yy, ⊥ is to zz in the previous discussion.

Then, the hydrostatic components leading to a shift of the average valence-band energy $\Delta E_{v,av}^{hy}$ (namely, $E_{v,av} = (E_{hh} + E_{lh} + E_{so})/3$) and the conduction band energy ΔE_c^{hy} can be described by:

$$\Delta E_{v,av}^{hy} = a_v\left(2\epsilon_{\parallel} + \epsilon_{\perp}\right), \qquad \Delta E_c^{hy} = a_c\left(2\epsilon_{\parallel} + \epsilon_{\perp}\right). \tag{2. 22}$$

where a_v and a_c are the hydrostatic deformation potentials for the valence and conduction band, respectively.

On the other hand, the shear strain contribution leading to an additional splitting of the valence-band energies associated with the split-orbit energy Δ_0 is described by:

$$\Delta E_{hh}^{sh} = -\frac{1}{2}\delta E^{sh} \quad . \tag{2. 23}$$

$$\Delta E_{lh}^{sh} = -\frac{1}{2}\Delta_0 + \frac{1}{4}\delta E^{sh} + \frac{1}{2}\sqrt{{\Delta_0}^2 + \Delta_0\delta E^{sh} + \frac{9}{4}\left(\delta E^{sh}\right)^2}. \tag{2. 24}$$

$$\Delta E_{so}^{sh} = -\frac{1}{2}\Delta_0 + \frac{1}{4}\delta E^{sh} - \frac{1}{2}\sqrt{{\Delta_0}^2 + \Delta_0\delta E^{sh} + \frac{9}{4}\left(\delta E^{sh}\right)^2}. \tag{2. 25}$$

where the strain-dependent shift δE^{sh} caused by a (001)-oriented substrate follows:

$$\delta E^{sh} = 2b\left(\epsilon_{\perp} - \epsilon_{\parallel}\right). \tag{2. 26}$$

b is defined as the tetragonal shear deformation potential.

Once the absolute value of the average valence-band energy $E_{v,av}$ is determined, using the above equations, we can obtain the valence-band and conduction-band edges E_v and E_c on an absolute scale from:

$$E_v = E_{v,av} + \frac{\Delta_0}{3} + \Delta E_{v,av}^{hy} + \max\left(\Delta E_{hh}^{sh}, \Delta E_{lh}^{sh}\right), \tag{2. 27}$$

$$E_c = E_{v,av} + \frac{\Delta_0}{3} + E_g + \Delta E_c^{hy}. \tag{2. 28}$$

Please notice that the average valence-band energy $E_{v,av}$, spin-orbit splitting energy Δ_0 and bandgap energy E_g are quantities in the absence of strain.

2.4 Essence knowledge on epitaxial layers

In this section, we introduce the essential concepts of epitaxial layers that have been taken into account when encountering and involving the design and actual growth of epitaxial layers in this research.

2.4.1 Thermodynamics of Epitaxial Growth

Common epitaxial growth techniques based on gas phase to solid phase reaction include Metal-Organic Vapor Phase Epitaxy (MOCVD), Molecular Beam Epitaxy (MBE), and Halide Vapor Phase Epitaxy (HVPE). Through flowing gas-phase sources on top of a substrate heated moderately to the desired growth temperature, it is possible to transfer the gas-phase precursors to the solid phase on the substrate forming the epitaxial layer. Since the associated chemical reaction is essentially driven by the variation of their Gibss free energy, the mechanisms and compositions of resultant films of the chemical reaction can hence be predicted and analyzed with thermodynamics. It should be noticed that such a discussion on the basis of thermodynamics is general and applicable to all the aforementioned epitaxial growth techniques.

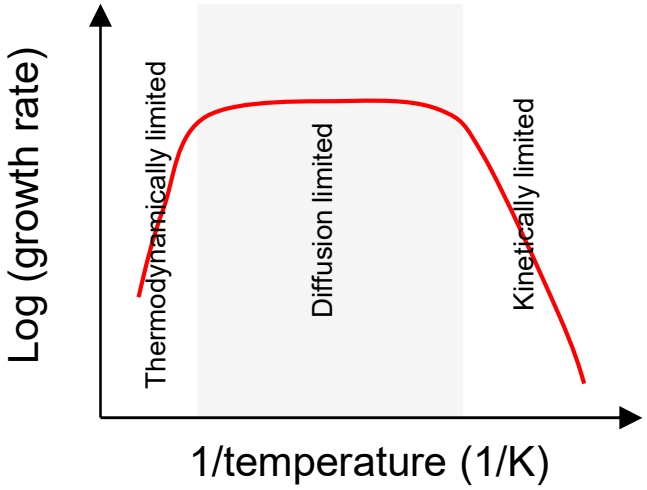

Figure 2. 4 The dependence of the growth rate on the growth temperature [10].

The processes behind vapor phase epitaxy involve in the mass transport of the reactants and the occurrence of reaction at the substrate surface, which can be summarized as below:

(1) Mass transport of the reactants to the growth region in the reaction chamber

(2) Diffusion of the reactants from the mainstream of the bulk gas to the substrate

(3) Attachment of the reactants to the surface of the substrate

(4) Nucleation reaction at the substrate surface

(5) The detachment of the reaction products

(6) Diffusion of the reaction products to the mainstream of the bulk gas flow

(7) Mass transport of the reaction products from the growth region in the chamber

The growth rate of the epitaxial layer is determined by the slowest process of the above reactions. For example, if the growth rate is limited by each of the (1), (2), (6), and (7) processes, it is referred to as the *mass transport limited regime*. On the other hand, if the process (3), (4), or (5) dominates the reaction rate, it is referred to as a *kinetically limited regime*. Figure 2. 4 illustrates the general features of the growth rate dependence on the reverse of growth temperature in the vapor phase epitaxy. At the low-temperature regime, as the growth temperature increases, the growth reaction increases drastically as well. This regime is recognized as a *kinetically limited regime*. Secondly, when the temperature increases to the moderately to the middle and to the high-temperature regime, it reaches the *mass transport limited regime*. In this case, theoretical analysis with thermodynamics becomes valid. According to the theory, if the nucleation reaction is much faster than the diffusion of the reaction precursors from the mainstream of the bulk gas flow, it can be assumed that the growth reaction involving the reactants arriving at the substrate surface reaches the equilibrium of the chemical reaction. In this sense, the partial pressure of each reactant at the substrate surface can be considered to be nearly equal to their pressure at equilibrium.

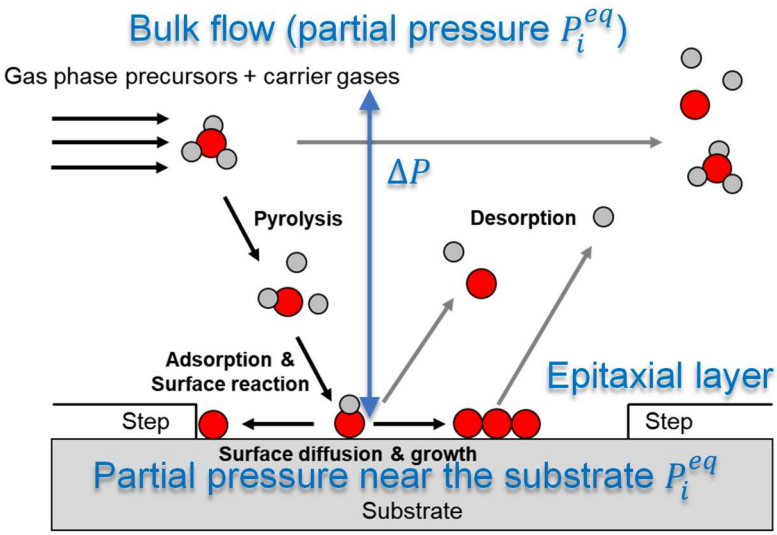

Figure 2. 5 Schematic of the thermodynamics of crystal growth of MOVPE, adapted from [11].

Then, the growth rate R_g can be approximated as follows:

$$R_g = K_g\left(P_i^0 - P_i^{eq}\right) = K_g \Delta P, \tag{2. 29}$$

where K_g is the so-called mass transport coefficient, P_i^0 is the partial vapor pressure of each precursor in the bulk gas mainstream, and P_i^{eq} is the equilibrium vapor pressure of the associated with each of the reactants, as depicted in Figure 2. 5. Here, the ΔP is identified as that property quantifying the driving force of the epitaxial growth. With a positive sign, the formation of epitaxial layers is expected to have a theoretical maximum growth rate described by the above formula. With a negative sign, if the last material grown on the substrate has the exact same materials for growing that layer, the etching process is expected to occur in this case.

In additional to the basic thermodynamics described previously, the growth rate of epitaxy based on MOCVD, in particular, reveals other crucial characteristics, i.e., proportional to the total partial pressure of group-III precursors, insensitive to a certain range of growth temperature, and uncorrelated with the ratio of the group-V supply to the group-III supply (or, V/III ratio). Because the precursors used for MOCVD (group-III supply, especially) are readily decomposed fully over 300 ˚C, the primary growth chemicals are considered to be completely reacted, and therefore the evaluation with thermodynamics is applicable. The commonly employed growth temperature range of

GaAs grown by MOCVD, for instance, is roughly located around 550 ˚C to 900 ˚C, which is considered to be satisfied with the theory.

Figure 2. 6 shows the diagram of solid composition versus input mole ratio for the quaternary InGaAsP alloys calculated by thermodynamics, where the growth temperature is 650 ˚C, V/III ratio is 10, and the partial pressure of group-III materials is 5×10^{-5} atm. The dashed lines indicate the alloy compositions lattice-matched to InP and GaAs substrates. Interestingly, it can be observed that the alloy compositions in the solid phase of group-III material (*Ga* and *In*) hold the exact ratios as in the gas phase, whereas for group-V material it turns out to be different. From this result, it can be seen that arsenic exhibits an extremely high incorporation rate in solid-phase than phosphors under the current growth condition. For example, even with input ratio As/(As + P) as low as 4 %, arsenic incorporation in solid-phase remains as high as 20 %, indicating the difficulty achieving InGaAsP (or, GaAsP) with high phosphors content at 650 ˚C. This manifests a significant, and typical behavior of III-V alloys. When doing the conditioning for epitaxial growth, the incorporation ratio of group-V elements in the solid phase tends to reveal a highly nonlinear relation to their ratio in the gas phase.

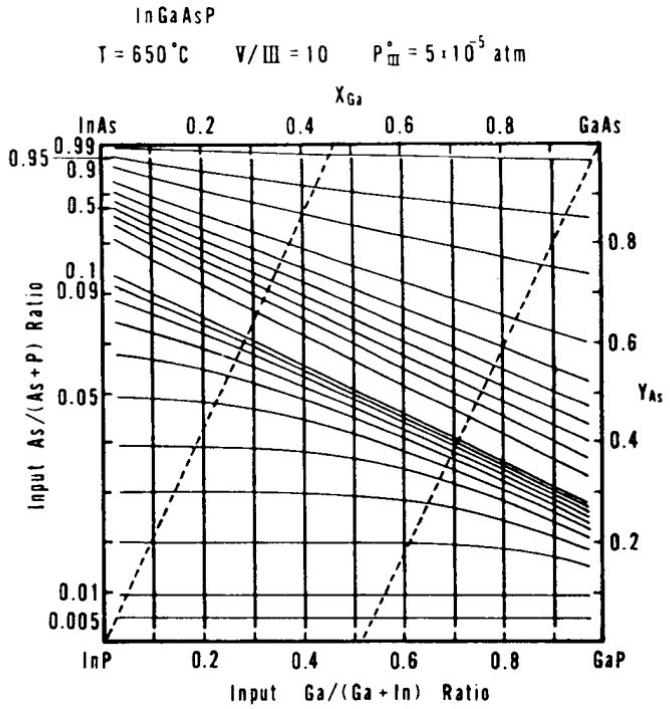

Figure 2. 6 The composition ratio in solid-phase versus input mole fraction for InGaAsP alloys. The dashed lines represent the lattice-matched conditions for InP and GaAs substrates [10].

2.4.2 Critical thickness

The critical thickness has always been an essential subject in heteroepitaxy. According to Frank and van der Merwe, as the thickness of the "pseudo-morphic" epitaxial layer increases, the strain energy accumulates proportionally and distributed homogeneously over the film initially. When the strain energy stored in the epitaxial layer exceeds a certain threshold, this excess cumulative energy tends to release to the generation of misfit dislocation. It is considered to be thermodynamically stable, as long as the thickness of the epitaxial layer doesn't go beyond a particular threshold known as the "critical thickness". In this section, two rigorous, and robust approaches for estimating the maximum available film thickness subjected to a uniformly distributed elastic strain are presented. These two methods have been widely employed when it comes to designing the desired thickness for various heterostructure optoelectronic devices, and thereby are taken into account in this research.

Matthews-Blakeslee critical thickness

Via balancing the force due to the line tension of misfit dislocation and the driving force from the elastic strain, Matthew and Blakeslee derived an explicit expression for the critical thickness. The derivation was based on a study of accommodation of misfit dislocation in epitaxial multilayers. It should be noted that such an assumption leads to the resulting critical thickness 4 times greater than that of a single epitaxial layer without additional layers on top, resulting from the strain sharing in two conjugate interfaces and the occurrence of a conjugate pair of misfit dislocations at these interfaces. In practice, the critical thickness for a single epitaxial layer by Matthew and Blakeslee is expressed as follow,

$$h_c = \frac{b}{8\pi f}\frac{1-\upsilon\cos^2\theta}{(1+\upsilon)\cos\lambda}\left(\ln\frac{h_c}{b}+1\right), \tag{2. 30}$$

where f is denoted for the lattice misfit (or, lattice-mismatch) between the epitaxial layer and the substrate, b is for its Burgers vector of the misfit dislocation, ν is for the Poisson's ratio, θ is for the angle between the dislocation line and the associated Burgers vector, and λ is for the angle between the slip direction and that direction in

the film plane which is perpendicular to the line of intersection of the slip plane and the interface. The Poisson's ratio can be evaluated by $C_{12} / (C_{11} + C_{12})$, where C represents the associated elastic constant.

People-Bean critical thickness

In contrast to the mechanically balanced assumption of the previous model, the critical thickness model proposed by People and Bean not only explicitly includes the effect from misfit dislocation, but also treats the issue by minimizing the free energy of the screw and edge dislocation of the epitaxial layer additionally. It is assumed that interfacial misfit dislocations will be generated when the areal strain energy density of the film exceeds the energy density associated with the generation of a screw dislocation at a distance from the free surface equal to the film thickness h. For epitaxial film thicker than this critical thickness h, screw and edge dislocations will be formed at the interface between the grown layer and the substrate. The People-Bean critical thickness is defined by:

$$h_c \approx \left(\frac{1-v}{1+v}\right)\left(\frac{1}{16\pi\sqrt{2}}\right)\left[\frac{b^2}{a(x)}\right]\left[\left(\frac{1}{f^2}\right)\ln\left(\frac{h_c}{b}\right)\right], \qquad (2.31)$$

where a is the lattice constant of the epitaxial layer, and f, b, and ν are the same as the symbol previously introduced.

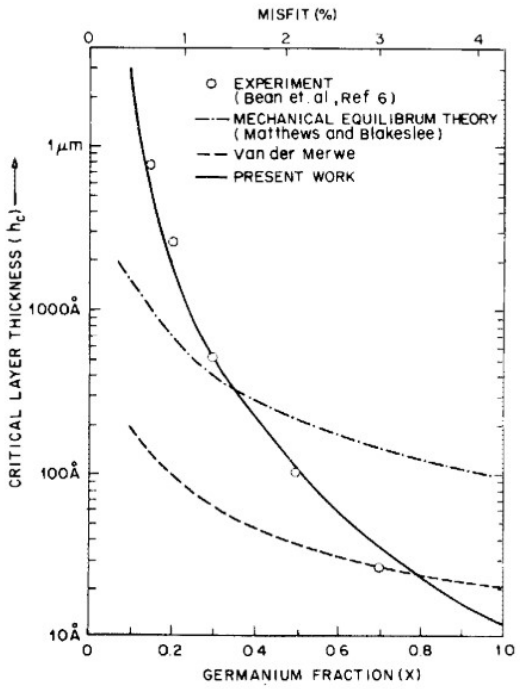

Figure 2. 7 Comparison of the People-Bean critical layer thickness (the solid curve) against the Blasklee-Matthew critical layer thickness [12].

The results obtained in the research are in excellent agreement with critical thickness measurements for Ge_xSi_{1-x} films on Si substrates, which was confirmed with crystal growth over the entire alloy composition range. As shown in Figure 2. 7, among all the presented models in the paper including the mechanical equilibrium Matthews-Blakeslee model, the energy equilibrium model by People and Bean remarkably agree with the experiment results. The most distinct difference between the Matthews-Blakeslee model and People-Bean model from the expression is the exponents of *f*, leading to the drastic discrepancy of the solved thicknesses in orders of magnitude in the lower misfit (< 1 %) and greater misfit (> 2 %) region.

In this research, we employ both criteria for examining whether the well and barrier thicknesses optimized by our proposed design framework for quantum well solar cells are feasible for epitaxial growth or not. Please noted that for *Zincblende* structure, θ and λ is equal to 60°. The magnitude of Burgers vector *b* is equal to $a/\sqrt{2}$, where *a* is the lattice constant.

2.4.3 Miscibility gap

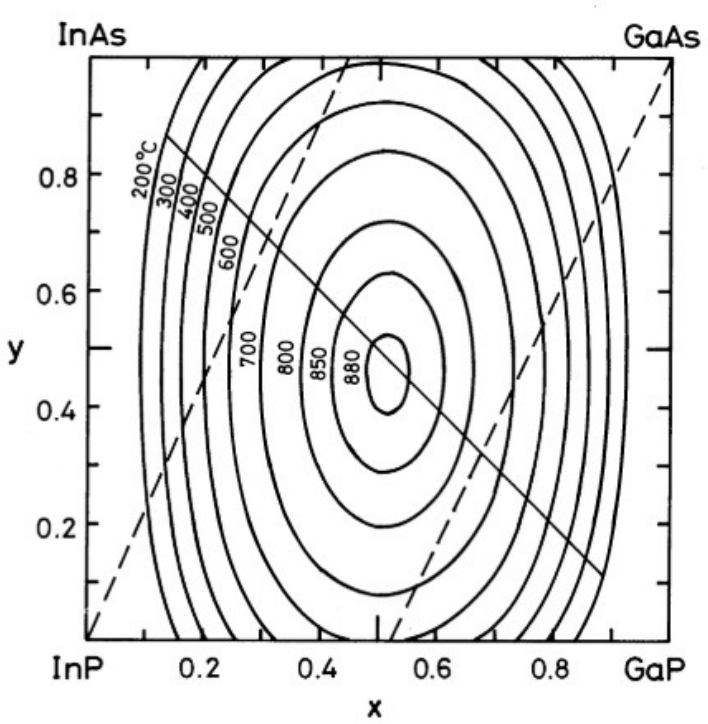

Figure 2. 8 Spinodal curves for InGaAsP (solid lines) at different growth temperatures. The dashed lines represent the lattice matching conditions for InP and GaAs. [13]

By adjusting the composition ratios of quaternary alloys, it has been considered as a promising approach to tune the bandgap energy of the material for various optoelectronic device applications. However, mixing binary constituents together may not be always thermodynamically stable depending on the growth temperature and the binary constituents of interests. This phenomenon is notoriously known as the so-called miscibility gap. For instance, quaternary InGaAsP alloys lattice-matched to GaAs substrate reveal theoretical bandgap energy ranging from 1.4 to 1.9 eV. Nonetheless, due to the substantial mismatch in the lattice constants and electron negativity among InP, InAs, GaP, and GaAs, the immiscible domain (gap) of the binary constituents presents, which limits composition range that can be synthesized as well as the tunability of bandgap energy. Figure 2. 8 illustrates the spinodal contour curves showing the immiscible domain for InGaAsP alloys at various temperatures by Onabe. Within the domain of each contour, phase separation will take place. It can be observed that only when the temperature exceeds 800 ˚C, the miscibility gap falls out of the

lattice-matched line for GaAs substrate (right dashed line). Although growth temperature as high as 800 ˚C is not practical for optoelectronic devices.

On the other hand, with the Delta-Lattice-Parameter (DLP) model developed by Stringfellow, one can roughly estimate the minimum demanded critical temperature above which the immiscible domain does not exist. For example, it is suggested that the critical temperature avoiding phase separation for InGaAsP, AlGaInP, and AlGaInAs are 908 K, 973 K, and 735 K respectively. Although it has been observed from the experiment results that this a sort of underestimation, these values can still serve as a basic reference when deciding the desired growth temperature.

In this research, refraining from the miscibility gap issue, we employ InGaP-well InGaP-barrier quantum wells as our design building blocks for solar cells, and InGaAs-well GaAsP-barrier quantum wells for designing the photonic power converter.

2.4.4 Strain-balanced Criteria

Solar cells as absorber normally require absorber thickness of micrometer order. Especially for quantum-well solar cells, the required absorber thickness tends to become much greater due to the less density of states for optical absorption compared to that of bulk materials. In this sense, to establish an overall stack thickness over a micrometer as a good absorber (i.e., the "overall critical thickness" of the stack), balancing the subjected compressive and tensile strain for the well and barrier layers is considered as a necessary condition designing the quantum well structures. For materials with a larger relaxed lattice constant than the substrate, the epitaxial layer will be subjected to a compressive strain on the substrate. On the contrary, for materials with a smaller relaxed lattice constant, it will be subjected to a tensile strain ("relaxed" means not pseudomorphically strained).

In the following discussion, the average lattice method, thickness weighted method, and zero-stress method for achieving a strain-balanced quantum-well design are introduced and compared. Here, we define a_{sub} as the lattice constant of the substrate, a_w and a_b as the relaxed lattice constants for well and barrier layers, t_w and t_b as the thicknesses for stacking the well and barrier layers, and A as the elastic stiffness coefficient. C as the elastic constant.

Average lattice method

It is suggested that a strain-balanced structure can be derived by forcing the thickness average of the compressive and tensile lattice constants to be equal to the lattice constant of substrate:

$$a_0 = \frac{t_w a_w + t_b a_b}{t_w + t_b}, \tag{2. 32}$$

Thickness weighted method

This method manifests that strain-balanced structure arises from forcing the thickness average of the compressive and tensile strain in a single-barrier single-well unit stack to be zero:

$$t_w \epsilon_w + t_b \epsilon_b = 0, \qquad a_{sub} = \frac{(t_w + t_b) a_w a_b}{t_w a_b + t_b a_w}, \tag{2. 33}$$

where strain ϵ_x is given by $(a_{\mathrm{sub}} - a_{\mathrm{x}})/ a_{\mathrm{x}}$.

On account of materials with different elastic parameters, the above relation can be further extended to be:

$$A_w t_w \epsilon_w + A_b t_b \epsilon_b = 0, \qquad a_{sub} = \frac{(A_w t_w + A_b t_b) a_w a_b}{A_w t_w a_b + A_b t_b a_w}, \tag{2. 34}$$

where the elastic stiffness coefficient is given by:

$$A = C_{11} + C_{22} - \frac{2C_{12}^2}{C_{11}}. \tag{2. 35}$$

Zero-stress method

The target of this model is to attain zero average in-plane stress in the tensile and compressively strained layer stack so that there is no shear force generated at the interfaces of the hetroepitaxy structure. Starting from obtaining the expression of the average in-plane stress from the average elastic energy density stored in the stack unit and letting it reach zero, yielding the strain-balanced condition:

$$A_w t_w \epsilon_w a_b + A_b t_b \epsilon_b a_w = 0, \qquad a_{sub} = \frac{A_w t_w a_w a_b^2 + A_b t_b a_b a_w^2}{A_w t_w a_b^2 + A_b t_b a_w^2}. \tag{2. 36}$$

It should be noticed that, while both average lattice and thickness weighted methods appear to be intuitive and straightforward, none of them are supported with any physics background.

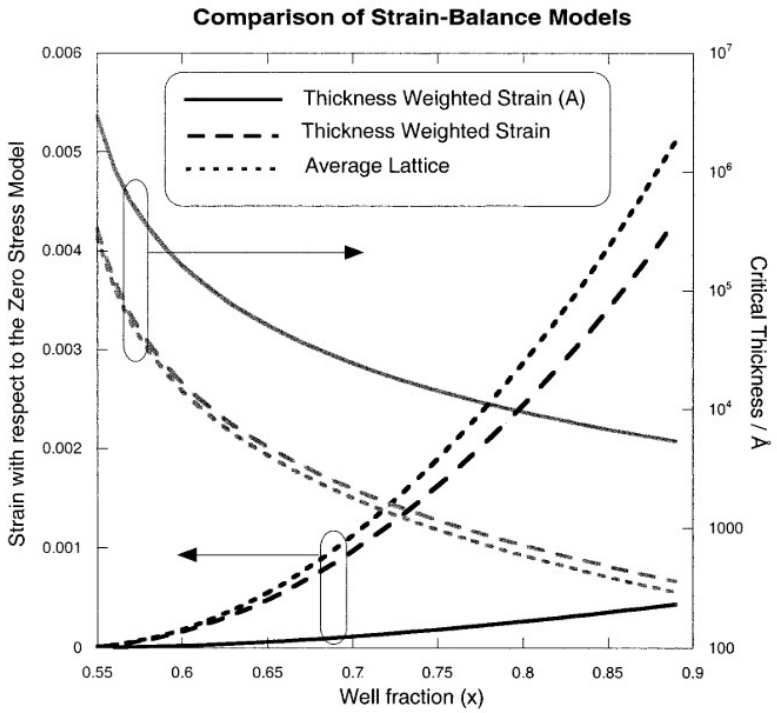

Figure 2. 9 Comparison of strain-balance models with respect to the zero-stress model [14].

Figure 2. 9 shows a comparison of the above models with a 10 nm-$In_xGa_{1-x}As$-well 10 nm-$In_yGa_{1-y}As$-barrier stack unit on InP substrate. According to the literature, the indium content y is firstly solved with the given x based on the zero-stress method. By substituting the x, y and the thicknesses into the average thickness model, thickness weighted model, and extended thickness weighted model, and using thickness average value to estimate the equivalent elastic parameters of the stack unit as a whole, both strain with respect to the zero-stress model and the associated critical stack thickness can be derived. As can be observed from Figure 2. 9, considering the elastic components in the model, the extended thickness weighted model exhibits the least cumulated strain and critical stack thickness with one order of magnitude larger than the other models especially at the relative highly-strained range ($x > 0.7$). In conclusion, the zero-stress method ensures a more accurate strain-balanced structure with high tolerance against defect formation and errors in growth parameters (i.e., the resulting material contents,

and the thicknesses of each layer). In this example, as high as the indium content of ~0.75 with less cumulated strain on the stack unit, the critical stack thickness above ~1 μm by the extended weighted strain model with respect to the zero-stress model holds a promising candidate serving as the thick absorber for solar cells.

In this research, we are interested in investigating a wide material content range that covers both slightly and highly strained cases. Distinguished from our previous research, the zero-stress method is adopted instead of the average lattice method and thickness weighted method, ensuring a more thermodynamically stable design as solar cells.

2.5 Ordering effects on InGaP alloy

Due to the rapid development of optoelectronic devices (e.g., lasers, LEDs…etc.), and high-speed high-power electronic devices (e.g., HBTs, HEMTs…etc.) based on III-V semiconductors, tailoring the composition contents of the alloy toward achieving high-performance devices had been a commonly employed technique in all the relevant research fields. Until the early 1980s, it had been believed that all the physical properties (e.g., bandgap energy, carrier mobility…etc.) of III-V semiconductors could be uniquely determined by the alloy composition of their group-III and group-V atoms, even if each group of atoms can distribute randomly on the associated sublattices. For example, no matter how the group-III *In* and *Ga* atoms distribute in $In_{1-x}Ga_xP$ on the group-III sublattice, it had been assumed that material properties such as the bandgap energy is a single-valued function of alloy composition *x*. Later on, however, it was discovered that the bandgap energy of $In_{0.49}Ga_{0.51}P$ in red-light laser diodes and *LED*s fabricated using *MOCVD* was almost 50 meV lower than the most reliable value of 1.91 eV obtained from a material grown using *liquid phase epitaxy* (*LPE*) regardless of the identical compositions of the *In* and *Ga* atoms. This means that even with a fixed composition *x* of 0.51, the bandgap energy of $In_{1-x}Ga_xP$ was not unique. According to transmission electron microscopy (*TEM*) measurement, the occurrence of alternating *Ga*-rich and *In*-rich atomic planes was revealed in the [-111] and [1-11] directions, resembling ordering in *CuPt* alloys. This kind of ordering is known as *CuPt*-B ordering, denoting the fact that only the (111)B planes are ordered. In fact, among all the categories of ordering in III-V semiconductors, *CuPt*-B ordering is one of the most

commonly observed atomic arrangements, which is also known as a sort of spontaneously formed superlattice. Theoretically speaking, when *CuPt*-B ordering occurs, this spontaneously formed superlattice induces effects such as the L-point of the Brillouin zone to fold back to the Γ-point and so on, leading to a narrowing of the bandgap energy.

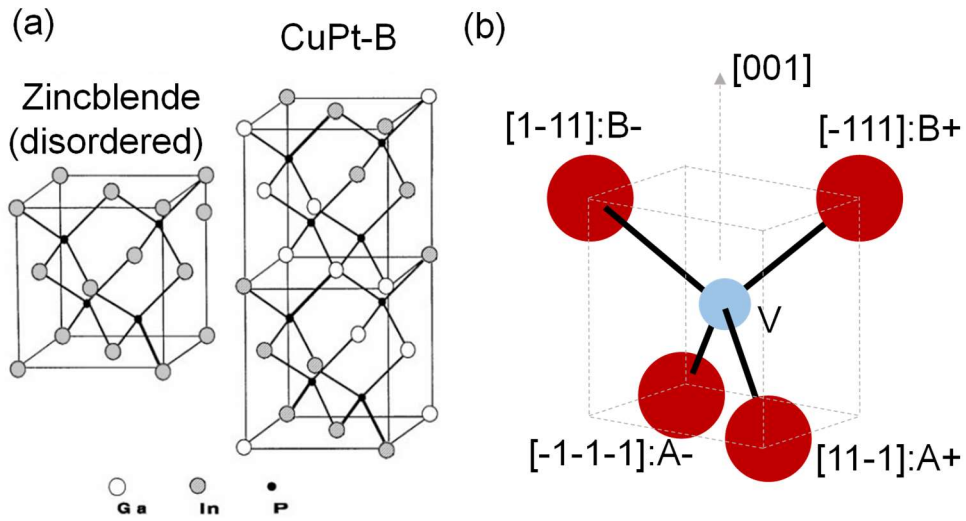

Figure 2. 10 (a) The unit cells of disordered and ordered GaInP. The group III lattice sites are randomly occupied by Ga and In-atoms in disordered GaInP [15]. (b) Schematic of the unit cell of a CuPt-B ordered crystal [16].

Figure 2. 10(a) shows the unit cell of disordered (left, *Zincblende* structure basically) and order InGaP (right). The Group-III atoms (*In*- and *Ga*-) randomly occupy the group-III site on the lattice. Figure 2. 10(b) depicts the structure model with the site convention of -*A* and -*B* sites denoted by the associated direction vectors [-111]:B+, [1-11]:B-, [11-1]:A+, and [-1-1-1]:A-.

Figure 2. 11 shows the transmission electron diffraction (*TED*) patterns of $In_{0.49}Ga_{0.51}P$ samples grown by *MOCVD* at 670 ˚C (a) on an exact (001)-oriented GaAs substrate, (b)(c) on an exact (001)-oriented GaAs substrate with etched [110] grooves taken from different domains of the sample (see reference). The area of the domain is reported to be several square micrometers. For both samples, the formation of both (-111) and (1-11) variants of the *CuPt* structure reveals that ordered $In_{0.49}Ga_{0.51}P$ was grown. On the other hand, the distinct intensities of the super spots (e.g., ½(-111), ½(1-11),…) relative to that of the *Zincblende* spots for the two samples reflect the distinct degrees of ordering under different growth conditions. In this case, the epilayer with grooves exhibits a higher degree of ordering.

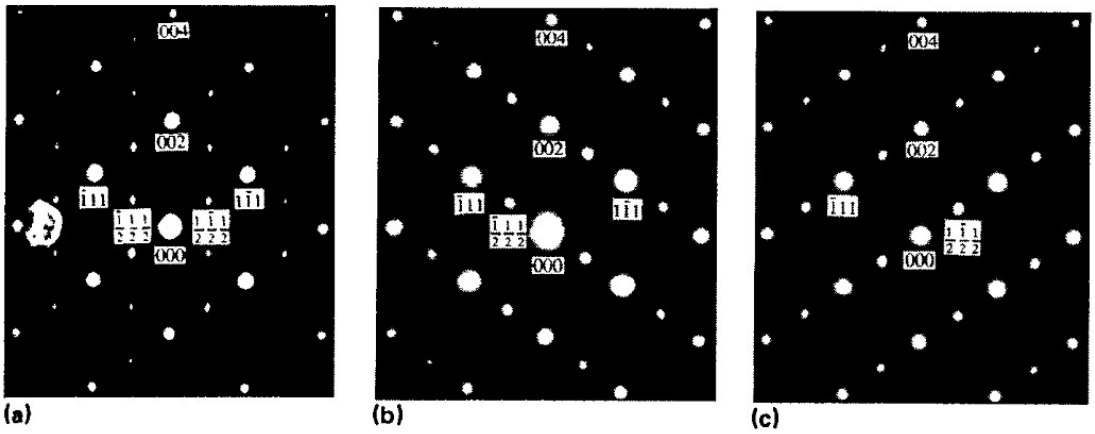

Figure 2. 11 Transmission electron diffraction pattern of $In_{0.49}Ga_{0.51}P$ samples grown on various oriented substrates [17].

In fact, by varying growth conditions, such as growth rate, V/III ratio, substrate orientation, and growth temperature, different degrees of the *CuPt*-B ordering of $In_{0.49}Ga_{0.51}P$ can be intentionally altered, as is summarized in Figure 2. 12. It is clear that the bandgap energy of $In_{0.49}Ga_{0.51}P$ characterized by the peak of photoluminescent measurement (although *PL* peak is not necessary to be exactly matched with the bandgap energy in general), due to the modification of electronic band structure caused by the ordering of the group-III atoms.

In the literature, phosphine was employed as the precursor gas of the group-V element, as indicated by the relatively high V/III ratio. The GaAs substrates adopted here were 2°-misoriented toward [011], which is fairly closed to (001). The V/III ratio was altered from 62 to 412 whereas the growth temperature was varied from 600 to 750 °C as shown in Figure 2. 12 (a). At high temperature, for example, 700 °C, as V/III ratio rises, the bandgap energy decreases, while at lower temperature such as 600 °C it goes the other way around.

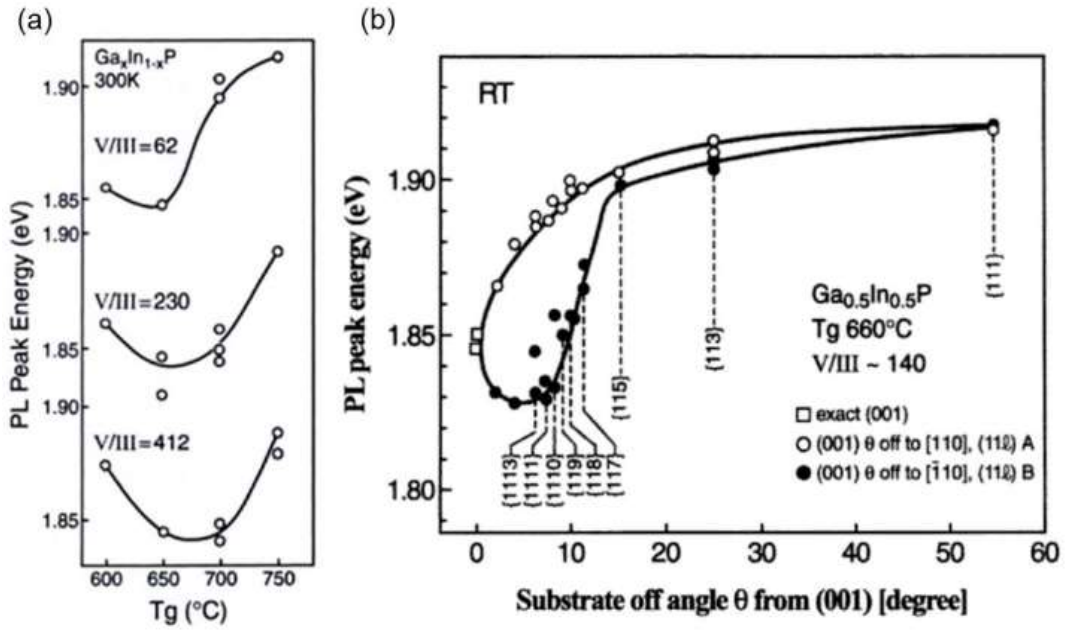

Figure 2. 12 (a) The dependence of the photoluminescent peak energy on the growth temperature and V/III-ratio and (b) orientation of the substrate of $Ga_{0.5}In_{0.5}P$ [16].

Additionally, as demonstrated in Figure 2. 12 (b), the effect of substrate orientation on *CuPt*-B ordering is quite intriguing as well. The bandgap energy measured at room temperature for $In_{0.49}Ga_{0.51}P$ grown by *MOCVD* at 660 ˚C on distinct misoriented GaAs substrate toward [-111] (B+) and [-1-1-1] (A-). The respective misorientation angle for each case is denoted by θ_B and θ_A. When θ_B increases from 0˚, the bandgap energy initially drops slightly until 6˚, and then rises rapidly as θ_B approaches 15˚ (nearly reaches the (-115) surface). When θ_B goes beyond 15˚ to 54˚ (or, the so-called (111)B surface), the bandgap energy goes gradually to 1.91 eV, the completely disordered case.

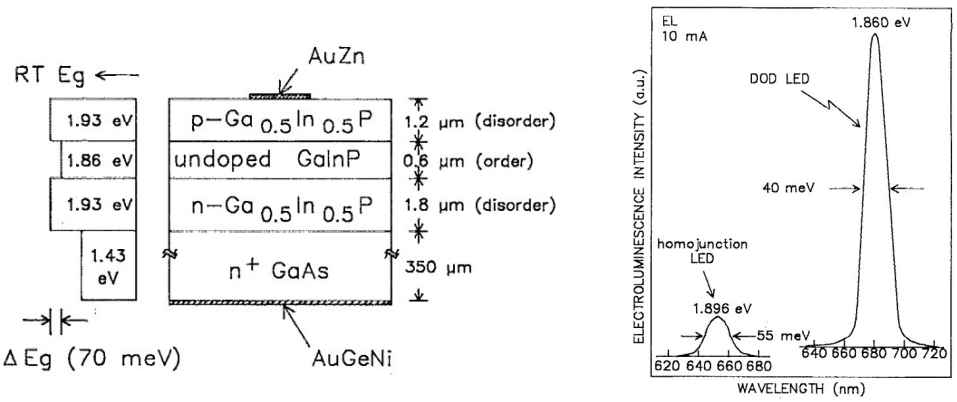

Figure 2. 13 Schematic of the disorder-order-disorder (DOD) LED as well as the band alignment (left) and the electroluminescence (EL) measurement result (right) [18], [19]. It should be noticed that the compositions of InGaP in the device are consistent.

Figure 2. 13 demonstrates an intriguing p-i-n double hetero-structure red LED composed of a disorder/order/disorder (DOD) proposed by Lee et al. in 1992. Via controlling the growth temperature and doping level for $In_{0.49}Ga_{0.51}P$, they proved that the electroluminescent (EL) efficiency can be improved or diminished significantly due to the presence of the ordering effects.

In this section, we discussed the *CuPt*-B ordering of $In_{0.49}Ga_{0.51}P$. Under various growth conditions, even with the identical composition ratio, physical properties such as bandgap energy could no longer be a unique value due to the ordering effects. In fact, alloys commonly adopted in the absorber layer, the window layer, or the back-surface field for solar cells, such as GaInP, AlInP, AlGaInP, and GaAsP, have been identified to present *CuPt*-B ordering, which implies its potential impact on the performance as solar cells. In this research, although, we do not take into account the ordering effects to avoid the redundant complexity when designing the quantum-well structures based on GaInP, one should always keep in mind that not only the conventional quantities (i.e., SRH-lifetime, background dopants, …) but the ordering effects may play a critical role in influencing the crystal quality and alloy properties of the exact fabricated devices, as indicated by the example in Figure 2. 13.

2.6 Reference

[1] S. Adachi, “Optical dispersion relations for GaP, GaAs, GaSb, InP, InAs, InSb, Al x Ga 1− x As, and In 1− x Ga x As y P 1− y,” *J. Appl. Phys.*, vol. 66, no. 12, pp. 6030–6040, Dec. 1989.

[2] S. Adachi, “Optical properties of In1-xGaxAs1-yPy alloys,” *Phys. Rev. B*, vol. 39, no. 17, pp. 12612–12621, Jun. 1989.

[3] M. C. Saleh, Bahaa EA and Teich, *Fundamentals of photonics*. John Wiley & Sons, 2019.

[4] Dresselhaus, MS, “Solid State Physics Part II Optical Properties of Solids,” *Lect. Notes (Massachusetts Inst. Technol. Cambridge, MA)*, vol. 17, 2001.

[5] I. Sayed and S. M. Bedair, “Quantum Well Solar Cells: Principles, Recent Progress, and Potential,” *IEEE J. Photovoltaics*, vol. 9, no. 2, pp. 1–22, 2019.

[6] J. Nelson, M. Paxman, K. W. J. Barnham, J. S. Roberts, and C. Button, “Steady-state carrier escape from single quantum wells,” *IEEE J. Quantum Electron.*, vol. 29, no. 6, pp. 1460–1468, Jun. 1993.

[7] H. Schneider and K. V. Klitzing, “Thermionic emission and Gaussian transport of holes in a GaAs/AlxGa1-xAs multiple-quantum-well structure,” *Phys. Rev. B*, vol. 38, no. 9, pp. 6160–6165, 1988.

[8] A. M. Fox, D. A. B. Miller, G. Livescu, J. E. Cunningham, and W. Y. Jan, “Quantum Well Carrier Sweep Out: Relation to Electroabsorption and Exciton Saturation,” *IEEE J. Quantum Electron.*, vol. 27, no. 10, pp. 2281–2295, 1991.

[9] S. L. Chuang, *Physics of photonic devices*. John wiley & Sons, 2009.

[10] Stringfellow, Gerald B, *Organometallic vapor-phase epitaxy: theory and practice*. Elsevier, 1999.

[11] K. Boram, “Heteroepitaxial metal-organic vapor phase epitaxy of III-V semiconductors on Si for high efficiency and low-cost solar cells,” The University of Tokyo, 2019.

[12] R. People and J. C. Bean, “Calculation of critical layer thickness versus lattice

mismatch for Ge xSi1-x/Si strained-layer heterostructures," *Appl. Phys. Lett.*, vol. 47, no. 3, pp. 322–324, 1985.

[13] K. Onabe, "Calculation of Miscibility Gap in Quaternary InGaPAs with Strictly Regular Solution Approximation," *Jpn. J. Appl. Phys.*, vol. 21, no. Part 1, No. 5, pp. 797–798, May 1982.

[14] N. J. Ekins-Daukes, K. Kawaguchi, and J. Zhang, "Strain-Balanced Criteria for Multiple Quantum Well Structures and Its Signature in X-ray Rocking Curves †," *Cryst. Growth Des.*, vol. 2, no. 4, pp. 287–292, Jul. 2002.

[15] F. Scholz *et al.*, "Ordering in GaInP: Is it relevant for devices?," *Phys. E Low-dimensional Syst. Nanostructures*, vol. 2, no. 1–4, pp. 8–14, Jul. 1998.

[16] A. M. Tohru Suzuki, *Spontaneous Ordering in Semiconductor Alloys*. 2002.

[17] G. S. Chen and G. B. Stringfellow, "Effects of step motion on ordering in GaInP," *Appl. Phys. Lett.*, vol. 59, no. 3, pp. 324–326, Jul. 1991.

[18] R. H. Horng and M. K. Lee, "Ordering effect on the performance of Ga 0.5 In 0.5 P visible light-emitting diodes grown by metalorganic chemical vapor deposition," *J. Appl. Phys.*, vol. 71, no. 3, pp. 1513–1516, Feb. 1992.

[19] M. K. Lee, R. H. Horng, and L. C. Haung, "Disorder/order/disorder Ga0.5In0.5P visible light-emitting diodes," *J. Appl. Phys.*, vol. 72, no. 11, pp. 5420–5422, 1992.

Chapter 3 Experiment equipment

3.1 Metal-Organic Vapor Phase Epitaxy (MOVPE)

Metal-organic vapor phase epitaxy (MOVPE) is a process in which monocrystalline compound semiconductor layers are grown by the reaction of molecules in the gas phase on a heated substrate. Because of its capability of mass production of high-quality epitaxial layers and compatibility with a wide verity of precursors for III-V semiconductors, it has been widely employed in the industry and several research fields for device fabrication. The precursor injected in the reactor is carried by carrier gases such as hydrogen. Relying on the concentration gradient as well as the pressure gradient between the substrate, the precursor can diffuse on the heated substrate and thus the chemical reaction process for crystal growth can be launched. The schematic diagram of the MOVPE system employed in this research is depicted in Figure 3. 1. The liquid metalorganic precursors are contained in stainless containers called bubblers. Gas-phase sources at the saturated vapor pressure are extracted to the reactor by bubbling the liquid source with a highly-purified carrier gas. The saturated vapor pressure for each precursor depends on the holding temperature of the thermal bath that keeps the bubblers, following the Antoine equations:

$$\log_{10} p_{sat}[\mathrm{Torr}] = A - \frac{B}{C+T}, \qquad (3.\ 1)$$

where T is the temperature of the bubbler. A, B and C are Antoine parameters. C is assumed to be zero for simplicity in this research. The precursors used in this research are: trimethylgallium (TMGa: $(CH_3)_3Ga$), trimethylindium (TMIn: $(CH_3)_3In$) and Trimethylaluminum (TMAl: Trimethylaluminum) for the group-III sources, and tertiarybutylarsine (TBAs: $(CH_3)_3CAsH_2$) and tertiarybutylphosphine (TBP: $(CH_3)_3CPH_2$) for group V sources. For p-type and n-type dopants, dimethylzinc (DMZn: $(CH_3)_2Zn$) and tellurium are used, respectively. The Antoine parameters A, B, melting points TM, boiling point TB for each bubbler, and the holding temperatures and pressures in the experiments in this study are summarized in the Table 3-1.

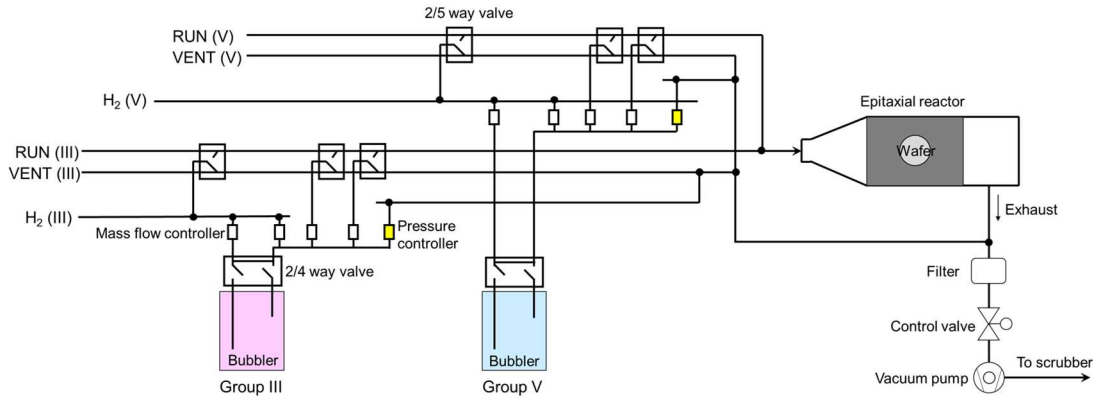

Figure 3. 1 Schematic diagram of the MOVPE system employed in this research [1].

Table 3.1 Properties of metal-organic precursors used in this research [2].

Source	A	B	T_M (°C)	T_B (°C)	$T_{bubbler}$ (°C)	$P_{bubbler}$ (mbar)
TMGa	8.07	1703	-15.8	55.8	17.0	1000
TMIn	10.52	3014	88.4	133.8	17.0	400
TMAl	8.224	2135	15.4	127	17.0	1000
TBAs	7.243	1509	-1	69	17.0	1000
TBP	7.586	1539	4	56.1	17	1000
DMZn	7.802	1560	-42	46	-10.0	1000

3.2 X-ray diffraction (XRD)

With a short wavelength of X-ray comparable to the target sample, the crystal structure and the detailed information epitaxial layers are resolved by using a diffractometer based on X-ray diffraction. The theory in X-ray diffraction relies on the elastic scattering of the incident X-ray from the atoms in the crystal lattice. According to Bragg's diffraction theory, the diffractive X-ray is constructively interfered and thus can be observed from its far-field pattern, as the following relation is fulfilled:

$$2d_{hkl}\sin\theta = n\lambda \ , \tag{3. 2}$$

where d_{hkl} is the spacing between the (h k l) planes of the atomic planes in the crystal lattice, n is an integer that indicates the order of the diffractive wave, λ is the wavelength of the incident X-ray. The schematic of the basic principle is illustrated in Figure 3. 2(a) where the atomic plane of the target sample is separated with a distance d.

By taking the advantage of its high resolving power, the fine structure of the samples such as the material compositions and the thickness of epitaxial layers, and the quality of the grown crystals in terms of mosaicity and the extent of lattice relaxation can be derived by fitting the measured diffraction pattern with a simulation pattern. Figure 3. 2(b) demonstrates a standard setup of a diffractometer composed of an X-ray source (X-ray generator, or a goniometer) and a 2θ-detector. These two components are mounted on two independent arms that can rotate freely for different purposes of measurement. Three typical scan schemes are summarized as follows:

(1) $\omega - 2\theta$ scan: A radial scan also known as $2\theta - \omega$ scan. Both ω-axis and 2θ-axis are rotated at the same speed. The incident angle is not identical to the exit angle of the X-ray. This scheme is adopted for analyzing the material content as well as the thicknesses of the grown samples in this research.

(2) 2θ scan: A radial scan also known as $2\theta - \theta$ scan. The exit angle is equal to the incident angle of the X-ray. The scattering angle is the same as the scanned angle of the 2θ detector.

(3) ω scan: A transverse also known as the X-ray rocking curve (XRC) scan. In this case, the scattering angle measured by controlling the 2θ-axis is fixed, whereas the incident angle controlled by the ω-axis is scanned.

More detailed information can be found in Ref. [3], [4].

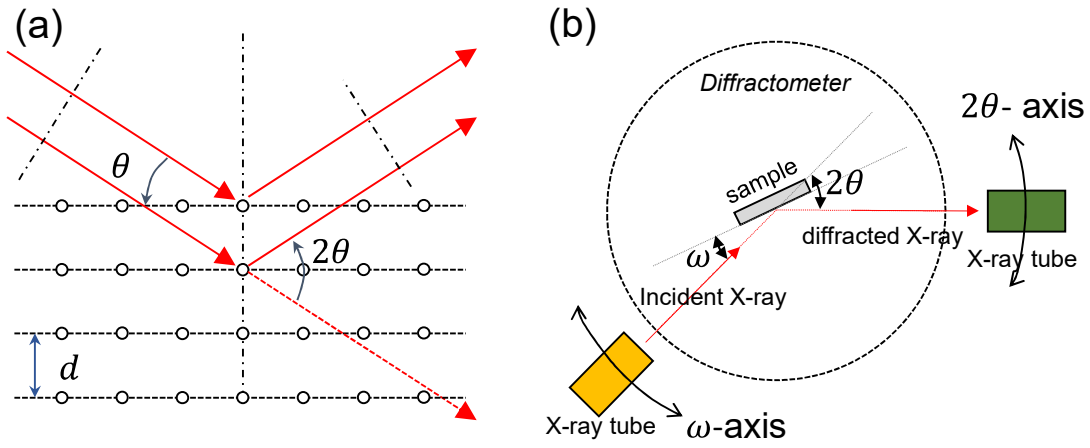

Figure 3. 2 (a) Principle of X-ray diffraction (XRD) from a crystal with atomic plane spacing by d. (b) Schematic of a typical diffractometer setup for XRD measurement.

3.3 Solar simulator

The characterization of a photovoltaic device is done by using a solar simulator in this research. Significant profiles of the I-V curve and quantum efficiency (QE) are determined by using a setup as shown in Figure 3. 3 (CEP-2000LS, Bunkokeiki).

A xenon lamp with 150 W for I-V measurement is utilized as the light source. An AM1.5G filter (100 mW/cm^2) is inserted along the optical path to produce a spectrum with resembled features of one-sun. On the other hand, the measurement for quantum efficiency is performed by using another xenon lamp with 300 W. The incident light is firstly monochromated and then passes thought a neutral-density filter (ND filter) so that consistent intensity of 2.5 mW/cm^2 is illuminated on the solar cell. In the monochromator, the reciprocal linear dispersion of the diffraction grating is 6 nm/mm. The slit width is set to be 4 mm to ensure a sufficient incident intensity, which corresponds to a resolution of 24 nm in the QE spectra. To ensure accuracy for the QE measurement under sunlight, the AM1.5G output is employed as the bias illumination. Due to the relatively low power of the monochromatic light compared to AM1.5G, the QW is measured in AC mode with a lock-in amplifier as well as a chopper. In this case, the current signal is converted into a voltage signal as the input signal. The setup is arranged for a four-terminal measurement. Therefore, the bias voltage of the solar cell is independently adjusted by using the source meter.

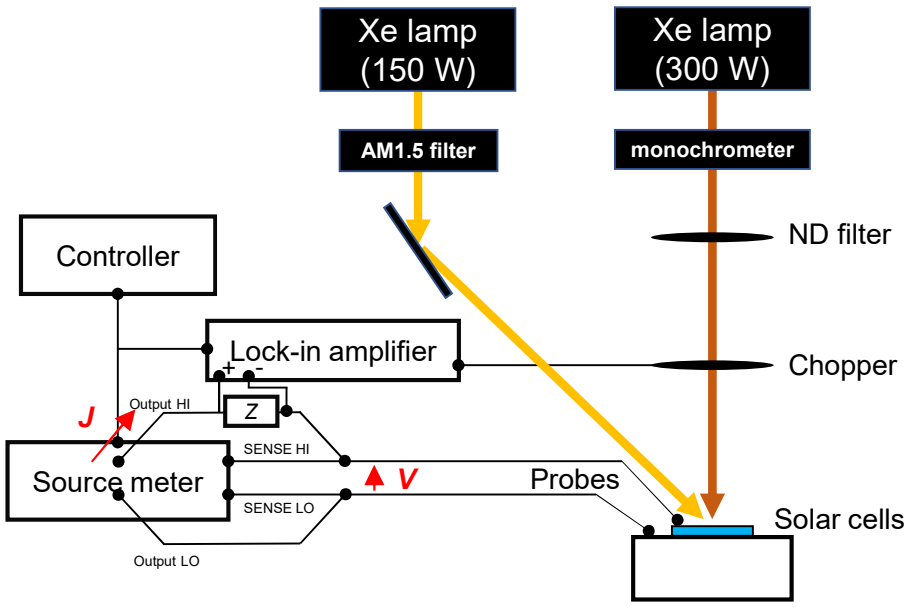

Figure 3. 3 Schematic of a solar simulator setup employed in this research.

3.4 Reference

[1] K. Boram, “Heteroepitaxial metal-organic vapor phase epitaxy of III-V semiconductors on Si for high efficiency and low-cost solar cells,” The University of Tokyo, 2019.

[2] Stringfellow, Gerald B, *Organometallic vapor-phase epitaxy: theory and practice*. Elsevier, 1999.

[3] Bowen, David Keith, Tanner, Brian K, *High resolution X-ray diffractometry and topography*. CRC press, 1998.

[4] Holy, Vaclav, Baumbach, Tilo, Pietsch, Ullrich, *High-resolution X-ray scattering from thin films and multilayers*. Springer, 1999.

List of Publications

Journal paper

Journal

First author

Co-author

[1] A. Ren, H. Xu, J.Q. Zhang, **H. H. Huang**, A. Delamarre, K. Watanabe, J. Q. Zhang, L. L. Wu, C. Liu, and M. Sugiyama, "Spatially Resolved Identification of Shunt Defects in Thin Film Solar Cells via Current Transport Efficiency Imaging Combined with 3D Finite Element Modeling", Solar RRL, 1800342, 2019.

Conference

International conference

First author

[1] **H. H. Huang**, K. Toprasertpong, M. M. Wilkins, K. Hinzer, M. Sugiyama, and Y. Nakano, "Trade-off Study on the Radiative Efficiency and Carrier Transport of Multiple-Quantum-Well Solar Cells," Proc. SPIE, Physics, Simulation, and Photonic Engineering of Photovoltaic Devices IX, San Francisco, California, USA, Feb. 2020.

[2] **H. H. Huang**, K. Toprasertpong, A. Delamarre, K. Watanabe, M. Sugiyama, and Y. Nakano, "Numerical Demonstration of Trade-off between Carrier Confinement Effect and Carrier Transport for Multiple Quantum Well Based High-efficiency InGaP Solar Cells," Compound Semiconductor Week (CSW), Nara, Japan, May 2019.

[3] **H. H. Huang**, K. Toprasertpong, A. Delamarre, J. Z. Sun, K. Watanabe, M. Sugiyama, and Y. Nakano, "Effective mobility map for InGaP/InGaP multiple quantum-well-based solar cells," Proc. SPIE 10913, Physics, Simulation, and Photonic Engineering of Photovoltaic Devices VIII; 1091310, San Francisco, California, USA, Feb. 2019.

Co-author

[1] M. M. Wilkins, **H. H. Huang**, H. Sodabanlu, M. Sugiyama, and K. Hinzer, "Laser power conversion at 977 nm using InGaAs/GaAsP multi-quantum-wells," Optical and Wireless Power Transmission Conference (OWPT2020), Yokohama, Japan, Apr. 2020.

[2] M. M. Wilkins, M. Asami, **H. H. Huang**, K. Hinzer, and M. Sugiyama, "p-i-p structure for time-of-flight measurements of effective carrier mobility in multi-

quantum-well structures," Proc. SPIE, Physics, Simulation, and Photonic Engineering of Photovoltaic Devices IX, San Francisco, California, USA, Feb. 2020.

International workshop

First author

[1] **H. H. Huang**, K. Toprasertpong, H. Sodabanlu, A. Delamarre, K. Watanabe, M. Sugiyama, and Y. Nakano, "Numerical and Experimental Demonstration of Multiple-Quantum-Well Design toward High-efficiency InGaP Solar Cells," Tsinghua - UT Joint Symposium, Beijing, China, May 2019.

[2] **H. H. Huang**, K. Toprasertpong, A. Delamarre, K. Watanabe, M. Sugiyama, and Y. Nakano, "Multiple quantum well Design toward High-Efficiency InGaP Solar Cells," LIMMS-Next PV Joint Energy Workshop, Tokyo, Japan, Mar. 2019.

Domestic conference

First author

[1] **H. H. Huang**, K. Toprasertpong, K. Watanabe, M. Sugiyama, and Y. Nakano, "A Study on the Limitation Factors of the Conversion Efficiency of Quantum Well Solar Cells," The 80th JSAP Autumn Meeting, Tokyo, Japan, Sept. 18-21, 2019.

[2] **H. H. Huang**, K. Toprasertpong, K. Watanabe, A. Delamarre, M. Sugiyama, and Y. Nakano, "Carrier Transport Modeling in Multiple Quantum Well Based InGaP Solar Cells," The 66th JSAP Spring Meeting, Tokyo, Japan, Mar. 9-12, 2019.